

Manuscript version: Published Version

The version presented in WRAP is the published version (Version of Record).

Persistent WRAP URL:

<http://wrap.warwick.ac.uk/170565>

How to cite:

The repository item page linked to above, will contain details on accessing citation guidance from the publisher.

Copyright and reuse:

The Warwick Research Archive Portal (WRAP) makes this work by researchers of the University of Warwick available open access under the following conditions.

Copyright © and all moral rights to the version of the paper presented here belong to the individual author(s) and/or other copyright owners. To the extent reasonable and practicable the material made available in WRAP has been checked for eligibility before being made available.






Copies of full items can be used for personal research or study, educational, or not-for-profit purposes without prior permission or charge. Provided that the authors, title and full bibliographic details are credited, a hyperlink and/or URL is given for the original metadata page and the content is not changed in any way.

Publisher's statement:

Please refer to the repository item page, publisher's statement section, for further information.

For more information, please contact the WRAP Team at: wrap@warwick.ac.uk

SN 2016iyc: a Type IIb supernova arising from a low-mass progenitor

Amar Aryan ^{1,2,★}, S. B. Pandey,¹ WeiKang Zheng,³ Alexei V. Filippenko,^{3,4} Jozsef Vinko,^{5,6,7,8} Ryoma Ouchi,⁹ Thomas G. Brink,³ Andrew Halle,³ Jeffrey Molloy,³ Sahana Kumar ^{3,10}, Goni Halevi ^{3,11}, Charles D. Kilpatrick ¹², Amit Kumar ^{1,13,14}, Rahul Gupta^{1,2} and Amit Kumar Ror¹

¹Aryabhata Research Institute of Observational Sciences, Manora Peak, Nainital 263002, India

²Department of Physics, Deen Dayal Upadhyay Gorakhpur University, Gorakhpur 273009, India

³Department of Astronomy, University of California, Berkeley, CA 94720, USA

⁴Miller Institute for Basic Research in Science, University of California, Berkeley, CA 94720, USA

⁵Department of Astronomy, University of Texas at Austin, Austin, TX 78712, USA

⁶CSFK Konkoly Observatory, Konkoly Thege M. ut 15-17, Budapest 1121, Hungary

⁷ELTE Eötvös Loránd University, Institute of Physics, Pázmány Péter sétány 1/A, Budapest 1117, Hungary

⁸Department of Optics and Quantum Electronics, University of Szeged, Dóm tér 9, Szeged 6720, Hungary

⁹Department of Astronomy, Kyoto University, Kitashirakawa-Oiwake-cho, Sakyo-ku, Kyoto 606-8502, Japan

¹⁰Department of Physics, Florida State University, Tallahassee, FL 32306, USA

¹¹Department of Astrophysical Sciences, Princeton University, 4 Ivy Lane, Princeton, NJ 08540, USA

¹²Center for Interdisciplinary Exploration and Research in Astrophysics and Department of Physics and Astronomy, Northwestern University, 1800 Sherman Avenue, 8th Floor, Evanston, IL 60201, USA

¹³School of Studies in Physics and Astrophysics, Pt. Ravishankar Shukla University, Chattisgarh 492010, India

¹⁴Department of Physics, University of Warwick, Gibbet Hill Road, Coventry CV4 7AL, UK

Accepted 2022 August 13. Received 2022 August 13; in original form 2022 January 19

ABSTRACT

In this work, photometric and spectroscopic analyses of a very low-luminosity Type IIb supernova (SN) 2016iyc have been performed. SN 2016iyc lies near the faint end among the distribution of similar supernovae (SNe). Given lower ejecta mass (M_{ej}) and low nickel mass (M_{Ni}) from the literature, combined with SN 2016iyc lying near the faint end, one-dimensional stellar evolution models of 9–14 M_{\odot} zero-age main-sequence (ZAMS) stars as the possible progenitors of SN 2016iyc have been performed using the publicly available code MESA. Moreover, synthetic explosions of the progenitor models have been simulated, using the hydrodynamic evolution codes STELLA and SNEC. The bolometric luminosity light curve and photospheric velocities produced through synthetic explosions of ZAMS stars of mass in the range of 12–13 M_{\odot} having a pre-supernova radius $R_0 = (204\text{--}300) R_{\odot}$, with $M_{\text{ej}} = (1.89\text{--}1.93) M_{\odot}$, explosion energy $E_{\text{exp}} = (0.28\text{--}0.35) \times 10^{51}$ erg, and $M_{\text{Ni}} < 0.09 M_{\odot}$, are in good agreement with observations; thus, SN 2016iyc probably exploded from a progenitor near the lower mass limits for SNe IIb. Finally, hydrodynamic simulations of the explosions of SN 2016gkg and SN 2011fu have also been performed to compare intermediate- and high-luminosity examples among well-studied SNe IIb. The results of progenitor modelling and synthetic explosions for SN 2016iyc, SN 2016gkg, and SN 2011fu exhibit a diverse range of mass for the possible progenitors of SNe IIb.

Key words: techniques: photometric – techniques: spectroscopic – supernovae: general – supernovae: individual: SN 2016iyc, SN 2016gkg, SN 2011fu.

1 INTRODUCTION

Type IIb supernovae (SNe) are a subclass of catastrophic core-collapse SNe (CCSNe). These SNe form a transition class of objects that link hydrogen (H)-rich Type II and H-deficient Type Ib SNe (Filippenko 1988; Filippenko, Matheson & Ho 1993; Smartt 2009; see Filippenko 1997 for a review). Their early phase spectra show strong H features, and distinct helium (He) lines start to appear a few weeks later; thus, these SNe are thought to be partially stripped by retaining a significant H envelope, and the He core is exposed once the envelope becomes optically thin.

The predominant powering mechanisms in SNe IIb are the radioactive decay of ^{56}Ni and the deposition of internal energy by the shock in the ejecta (e.g. Arnett 1980, 1982, 1996; Nadyozhin 1994; Chatzopoulos et al. 2013; Nicholl, Guillochon & Berger 2017). In a few cases, the SN progenitors are also surrounded by dense circumstellar material (CSM) that may interact violently with the SN ejecta. The interaction of CSM with the SN ejecta results in the formation of a two-component shock structure: a forward shock moving into the CSM and a reverse shock moving back into the SN ejecta. Both of these shocks deposit their kinetic energies into the material that is radiatively released, powering the light curves of the SNe (e.g. Chevalier & Fransson 1982, 1994; Moriya et al. 2011; Ginzberg & Balberg 2012; Chatzopoulos et al. 2013; Nicholl et al. 2017).

Understanding the possible progenitors of stripped or partially stripped CCSNe is a challenging task. Methods to investigate the

* E-mail: amar@aries.res.in, amararyan941@gmail.com

SN progenitors and their properties include (a) direct detections of objects in pre-explosion images, and (b) modelling of certain mass zero-age main-sequence (ZAMS) stars as the possible progenitors, based on the observed photometric and spectroscopic properties of the SNe. Direct detections of progenitors are rare owing to the uncertainty associated with the spatial positions and the infrequent occurrence of these transient phenomena. One has to be very lucky to get such pre-explosion images. However, for SNe IIB, four cases of the direct detection of objects in pre-explosion images have been claimed. These include SN 1993J (Filippenko 1993; Aldering, Humphreys & Richmond 1994), SN 2008ax (Crockett et al. 2008), SN 2011dh (Maund et al. 2011; Van Dyk et al. 2011), and SN 2013df (Van Dyk et al. 2014), indicating either massive Wolf–Rayet (WR) stars ($M_{\text{ZAMS}} \approx 10\text{--}28 M_{\odot}$; Crockett et al. 2008) or more extended yellow supergiants (YSGs) with $M_{\text{ZAMS}} = 12\text{--}17 M_{\odot}$ (Van Dyk et al. 2013; Folatelli et al. 2014; Smartt 2015) as SN IIB progenitors. Following Smartt et al. (2009) and Van Dyk (2017), there have only been ~ 34 cases of direct CCSNe progenitor detections. With these direct detections, the progenitors of SNe IIP are red supergiants (RSGs); SN IIn progenitors are luminous blue variables; the progenitors of SNe IIIc are still debated, with only the case of SN 2009kr suggesting RSG or yellow supergiant progenitors; and the progenitors of SNe Ib/c are either low-mass stars in a binary system (Podsiadlowski, Joss & Hsu 1992; Nomoto, Iwamoto & Suzuki 1995; Smartt 2009) or a single massive WR star (e.g. Gaskell et al. 1986; Eldridge, Langer & Tout 2011; Groh et al. 2013).

The second method, progenitor modelling using stellar evolution codes to constrain the nature of the possible progenitors of stripped or partially stripped CCSNe, identified either via direct imaging as in the case of iPTF13bvn (Cao et al. 2013) or indirect methods including nebular-phase spectral modelling (Uomoto 1986; Jerkstrand 2015), and simulating the synthetic explosions of their pre-SN models, is also vital to understand their nature, physical conditions, circumstellar environment, and chemical compositions. But the progenitor modelling of such objects using various stellar evolution codes is difficult owing to the complicated stages of shell burning. Another problem associated with such modelling is the obscure nature of the mixing-length-theory parameter (α_{MLT}). The basis of α_{MLT} has no physical origin (Joyce & Chaboyer 2018; Viani et al. 2018). Furthermore, Joyce & Chaboyer (2018) mentions that α_{MLT} is neither a physical constant nor a computational one; it is rather a free parameter, so the value of α_{MLT} must be determined individually in each stellar evolution code.

Owing to the above-mentioned difficulties, only a handful of such studies including progenitor modelling followed by their synthetic explosions have been performed in the case of stripped or partially stripped CCSNe, including the Type Ib SN iPTF13bvn (Cao et al. 2013; Bersten et al. 2014; Paxton et al. 2018), the famous Type IIB SN 2016gkg (Bersten et al. 2018), a few other Type IIB SNe including SN 2011dh (Bersten et al. 2012), SN 2011fu (Morales-Garoffolo et al. 2015), two Type Ib SNe 2015ap and 2016bau (Aryan et al. 2021), and another Type Ib SN 2012au (Pandey et al. 2021).

Considering these limited studies, our work goes one step further, as we perform the one-dimensional stellar evolution of the possible progenitors of the low-luminosity Type IIB SN 2016iyc and also simulate synthetic explosions. Our studies in this work point towards SN 2016iyc originating from the lower mass end of the ZAMS progenitor systems observed for Type IIB CCSNe.

This paper is divided into eight sections, including an introduction in Section 1. Section 2 provides details about various telescopes and reduction procedures, including the discovery of SN 2016iyc using the Katzman Automatic Imaging Telescope (KAIT) at Lick

Observatory as well as recalibrated photometry of SN 2016gkg. In Section 3, methods to correct for the extinction, photometric properties including the bolometric light curve, black-body temperature, and radius evolutions are discussed. We present the analyses describing the spectral properties and comparisons with other similar and well-studied SNe in Section 4; we also model the spectra of these SNe using SYN++. The assumptions and methods for modelling the possible progenitor of SN 2016iyc and the evolution of the models until the onset of core collapse using MESA are presented in Section 5. Further, in this section, we discuss the assumptions and methods for simulating the synthetic explosions using SNEC and STELLA. Here, comparisons between the parameters obtained through synthetic explosions and observed ones are presented. We also perform hydrodynamic modelling of the synthetic explosions of SN 2016gkg and SN 2011fu in Section 6. In Section 7, we discuss our major results and findings. We summarize our work and provide concluding remarks in Section 8.

2 DATA ACQUISITION AND REDUCTION

SN 2016iyc was discovered (de Kouchkovsky et al. 2016) in an 18 s unfiltered image taken at 03:28:00 on 2016 December 18 (UT dates are used throughout this paper) by the 0.76 m KAIT as part of the Lick Observatory Supernova Search (LOSS; Filippenko et al. 2001). Its brightness was 17.81 ± 0.11 mag, and the object was not detected earlier on 2016 December 04.14 with an upper limit of 19.0 mag. We measure its J2000.0 coordinates to be $\alpha = 22^{\text{h}}09^{\text{m}}14^{\text{s}}.29$, $\delta = +21^{\circ}31'17''.3$, with an uncertainty of $0''.5$ in each coordinate. SN 2016iyc is $14''.0$ west and $10''.4$ north of the nucleus of the host galaxy UGC 11924, which has redshift $z = 0.012685 \pm 0.000017$ (Giovanelli & Haynes 2016), with a spiral morphology (Sd). *B*, *V*, *R*, and *I* multiband follow-up images of SN 2016iyc were obtained with both KAIT and the 1 m Nickel telescope at Lick Observatory; KAIT also obtained additional unfiltered [*Clear* (*C*-band)] images. Although unfiltered and thus non-standard, *C* is most similar to the *R* band (Li et al. 2003), and has been widely used for SN observations by KAIT (e.g. de Jaeger et al. 2019; Stahl et al. 2019; Zheng et al. 2022).

All images were reduced using a custom pipeline¹ detailed by Stahl et al. (2019). Here, we briefly summarize the photometric procedure. Image subtraction was conducted in order to remove the host-galaxy contribution, using additional images obtained after the SN had faded below the detection limit. Point spread function (PSF) photometry was obtained, using DAOPHOT (Stetson 1987) from the IDL Astronomy User’s Library.² Several nearby stars were chosen from the Pan-STARRS1³ catalogue for calibration purpose; their magnitudes were first transformed into the Landolt (1992) system using the empirical prescription presented by Torny et al. (2012, equation 6), and then into the KAIT/Nickel natural system. All apparent magnitudes were measured in the KAIT4/Nickel2 natural system. The final results were transformed to the standard system using local calibrators and colour terms for KAIT4 and Nickel2 (Stahl et al. 2019).

The same method was adopted to reprocess the LOSS data of SN 2016gkg (originally published by Bersten et al. 2018), except that no subtraction procedure was applied to SN 2016gkg; the calibration source was also chosen from the Pan-STARRS1 catalogue. Photometry of SN 2016gkg at two epochs was also obtained with the

¹<https://github.com/benstahl92/LOSSPhotPipeline>

²<http://idlastro.gsfc.nasa.gov/>

³<http://archive.stsci.edu/panstarrs/search.php>

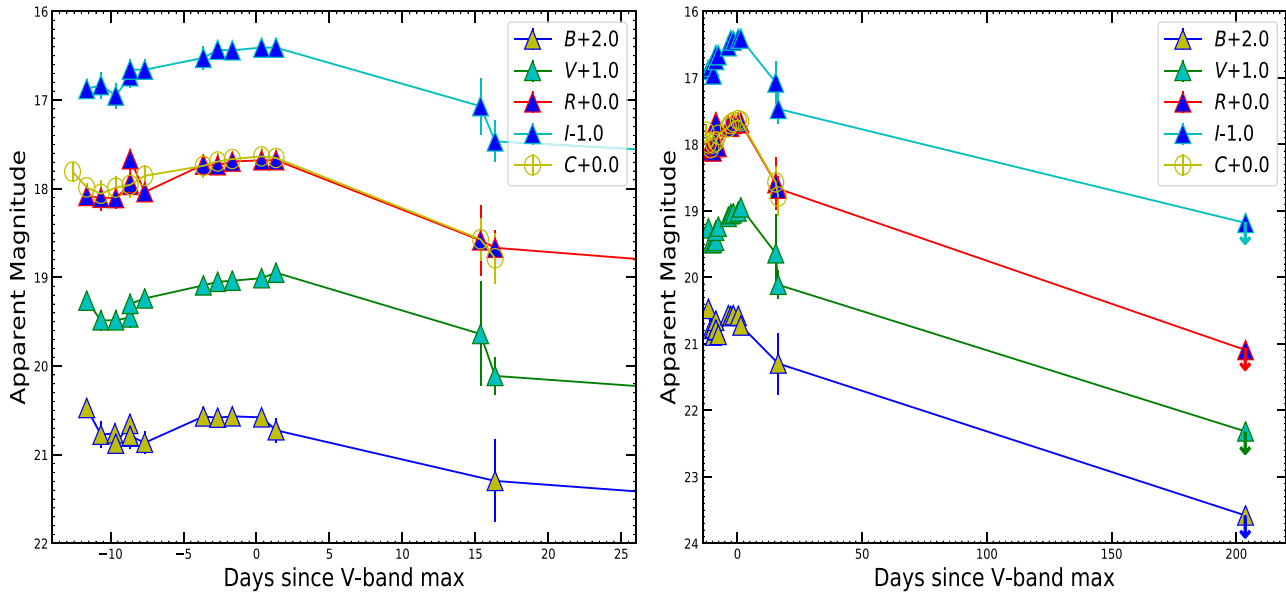


Figure 1. *Left:* The *BVRI*- and *C*-band light curves of SN 2016iyc, obtained with KAIT. The generic extended-SBO feature of SNe I Ib is visible in each band. *Right:* The *BVRI* and *C* light curves along with upper limits in each band using the Las Cumbres Observatory global telescope network. The upper limits in the last epoch are extremely useful for setting an upper limit on M_{Ni} .

3.6 m Devasthal optical telescope (DOT), using the $4\text{K} \times 4\text{K}$ CCD Imager (Pandey et al. 2018; Kumar et al. 2022). SN 2016gkg was the first SN detected by the 3.6 m DOT during its initial commissioning phases. For the data obtained from the 3.6 m DOT, the Landolt (1992) photometric standard fields PG 0918, PG 1633, and PG 1657 were observed on 2021 February 7 along with the SN field in the *UBVRI* bands under good photometric conditions. These three Landolt fields have standard stars with a *V*-band magnitude range of 12.27–15.26 mag and a $B - V$ colour range of -0.27 to $+1.13$ mag. The SN fields observed in 2021 were used for template subtraction to remove the host-galaxy contributions from the source images. Template subtraction was performed with standard procedures by matching the full width at half-maximum intensity (FWHM) and flux values of respective images. The optical photometric data reduction and calibration were made with a standard process discussed by Kumar et al. (2021) and PYTHON scripts hosted on REDPIPE (Singh 2021). The average atmospheric extinction values in the *U*, *B*, *V*, *R*, and *I* bands for the Devasthal site were adopted from Kumar et al. (2022). The recalibrated KAIT data of SN 2016gkg along with those observed at later epochs using the $4\text{K} \times 4\text{K}$ CCD Imager mounted at the axial port of the 3.6 m DOT were used for the construction of bolometric light curves as described in the following sections.

A single optical spectrum of SN 2016iyc was obtained on 2016 December 23 with the Kast double spectrograph (Miler & Stone 1993) mounted on the 3 m Shane telescope at Lick Observatory. The 2700 s exposure was taken at or near the parallactic angle to minimize slit losses caused by atmospheric dispersion (Filippenko 1982). The observations were conducted with a 2 arcsec-wide slit, 600/4310 grism on the blue side, and 300/7500 grating on the red side. This instrument configuration has a combined wavelength range of ~ 3500 – $10\,400$ Å and spectral resolving power of $R \approx 800$. Data reduction followed standard techniques for CCD processing and spectrum extraction (Silverman et al. 2012) utilizing IRAF⁴ routines and custom

PYTHON and IDL codes.⁵ Low-order polynomial fits to comparison-lamp spectra were used to calibrate the wavelength scale, and small adjustments derived from night-sky lines in the target frames were applied. Observations of appropriate spectrophotometric standard stars were used to flux calibrate the spectrum.

3 PHOTOMETRIC PROPERTIES

In this section, we discuss the photometric properties of SN 2016iyc, including the colour evolution, extinction, bolometric light curves, and various black-body parameters. The *BVRI*- and *C*-band photometric data of SN 2016iyc are presented in Table A1.

Most of the analyses in this paper have been performed with respect to the phase of *V*-band maximum brightness. The photometric data of SN 2016iyc lack dense coverage near peak brightness; thus, to find the phase of *V*-band maximum, we used the *V*-band light curve of SN 2013df as a template having a rising time-scale similar to that of SN 2016iyc (Fig. A1). We fit a fourth-order polynomial to the template light curve and find the date of *V* maximum to be $\text{MJD } 57752.7 \pm 0.2$. The left-hand panel of Fig. 1 shows the *BVRI*- and *C*-band light curves of SN 2016iyc. The characteristic extended shock-breakout (hereafter, extended-SBO) feature typically observed in SNe I Ib is seen in all of the bands. Multiple mechanisms and/or ejecta/progenitor properties have been theorized to explain such enhancement in the luminosity before the primary peak, including an increase in the progenitor radius up to a few $100 R_{\odot}$ (e.g. Nomoto et al. 1993; Podsiadlowski et al. 1993; Woosley et al. 1994); an interaction with CSM similar to the case of Type IIc SNe (Schlegel 1990); in a close-binary system, the interaction with the companion (Kasen & Bildsten 2010; Moriya, Liu & Izzard 2015); and sometimes enhanced ^{56}Ni mixing into the outer ejecta (e.g. Arnett & Fu 1989). The right-hand panel of Fig. 1 shows the *BVRI* and *C* light curves along with the late-time upper limits in each band. These upper limits are very useful in constraining the upper limit on M_{Ni} .

⁴IRAF is distributed by the National Optical Astronomy Observatory, which is operated by AURA, Inc., under a cooperative agreement with the US NSF.

⁵<https://github.com/ishivvers/TheKastShiv>

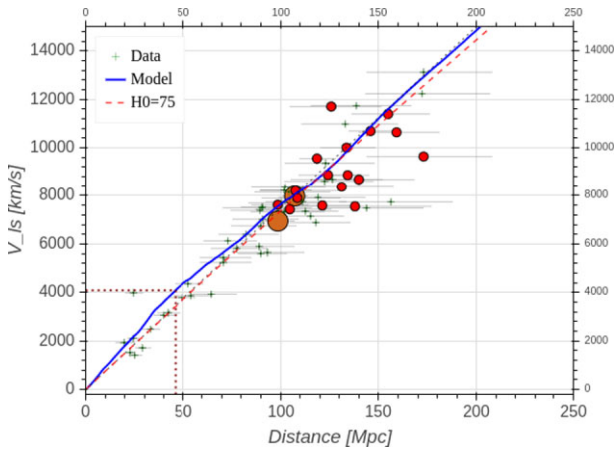


Figure 2. Distance estimation for the nearby ($z = 0.012685$) SN 2016iyc field ($\alpha = 22^{\text{h}}09^{\text{m}}14^{\text{s}}.29$, $\delta = +21^{\circ}31'17''.3$), using the method described by Kourkchi et al. (2020) with Graziani et al. (2019) models. The distance value estimated with this method is ~ 10 Mpc (~ 20 per cent) nearer than that reported using the published redshift value (Planck Collaboration XIII 2016) for SN 2016iyc.

3.1 Distance estimation of SN 2016iyc

Distance determinations from redshifts (z) are severely biased for nearby SNe because of the peculiar motions of nearby galaxies that are comparable to the Hubble flow. So, the redshift-based distance estimates can be used only for SNe having $z > 0.1$. Hence, the redshift-based distance for SN 2016iyc, published by Planck Collaboration XIII (2016), could be spurious. SN 2016iyc being nearby ($z = 0.012685$), we cross-verified the redshift-based distance estimate (56.6837 Mpc as mentioned by Planck Collaboration XIII 2016) with an advanced tool (Fig. 2) recently featured by Kourkchi et al. (2020),⁶ known as the Distance-Velocity ($D-V$) Calculator. Corresponding to a heliocentric velocity $V_h \approx 3804 \text{ km s}^{-1}$, the observed velocity (V_{ls}) at the location of SN 2016iyc is found to be $\sim 4089 \text{ km s}^{-1}$ by utilizing equation (5) of Kourkchi et al. (2020). Corresponding to $V_{\text{ls}} = 4089 \text{ km s}^{-1}$, the $D-V$ Calculator gives a distance of ~ 46 Mpc, which is ~ 20 per cent less than Planck Collaboration XIII (2016). The distance modulus for SN 2016iyc corresponding to this distance is 33.31 mag and is adopted for all further analyses in this paper. The distances for the SNe used as a comparison sample are well established in the literature and are used as such for the estimation of their respective bolometric luminosities. The distance of each SN in the comparison sample along with the corresponding distance modulus is presented in Table 1.

3.2 Colour evolution and extinction correction

For SN 2016iyc, we corrected for the Milky Way (MW) extinction using NED, following Schlafly & Finkbeiner (2011). In the direction of SN 2016iyc, $E(B - V)_{\text{MW}} = 0.067$ mag, so the MW extinction corrections for the B , V , R , and I bands are 0.278, 0.207, 0.155, and 0.099 mag, respectively.

Only one spectrum of SN 2016iyc is available, and it does not exhibit a clear Na ID absorption line produced by gas in the host galaxy, suggesting that there is negligible host-galaxy extinction. However, neglecting host-galaxy extinction based on only the absence of obvious Na ID could be spurious. In a recently published

Lick/KAIT data-release paper for various stripped-envelope SNe, Zheng et al. (2022) performed comprehensive analysis to determine the host-galaxy contamination and found $E(B - V)_{\text{host}} = 0.07$ mag for SN 2016iyc. We also performed a simple analysis to put an upper limit on the host-galaxy extinction. Five early epochs were selected, and the spectral energy distribution (SED) was fitted with black-body curves by assuming different $E(B - V)_{\text{host}}$ values (Fig. A2). We found that going beyond 0.07 mag of host-galaxy extinction results in black-body temperature exceeding 11 200 K. Such high temperatures are generally not seen in SNe IIB. Following Ben-Ami et al. (2015), the early-time black-body temperatures associated with SN 1993J, SN 2011dh, and SN 2013df are 8200, 8200, and 7470 K, respectively. There have been only a few cases where the early black-body temperature exceeds 11 000 K; one such example is SN 2001ig Ben-Ami et al. (2015), but this SN may have come from a compact WR binary progenitor system (Ryder et al. 2004).

Based on the above analyses and the results of Zheng et al. (2022), we adopt a host-galaxy extinction of 0.07 mag throughout this paper. Thus, a total (Milky Way + host-galaxy) extinction of $E(B - V)_{\text{tot}} = 0.137$ mag is adopted for SN 2016iyc. Fig. 3 shows the comparison of total extinction corrected $(B - V)_0$ colour of SN 2016iyc with other similar SNe.

3.3 Bolometric light curves

Before computing the bolometric light curves, the absolute V -band light curve of SN 2016iyc is compared with a few other similar SNe IIB. The left-hand panel of Fig. 4 shows that SN 2016iyc lies towards the fainter end of the distribution.

Furthermore, to obtain the quasibolometric light curve, we make use of the SUPERBOL code (Nicholl 2018). The extinction-corrected B , V , R , and I data are provided as input to SUPERBOL. The light curve in each filter is then mapped to a common set of times through the processes of interpolation and extrapolation. Thereafter, SUPERBOL fits black-body curves to the SED at each epoch, up to the observed wavelength range (4000–9000 Å), to give the quasibolometric light curve by performing trapezoidal integration.

The right-hand panel of Fig. 4 shows the comparison of the quasibolometric light curve of SN 2016iyc with other well-studied SNe IIB as listed in Table 1. The peak quasibolometric luminosity ($\log(L_{\text{BVRI}})_p$) of each SN has also been calculated by fitting a third-order polynomial to the quasibolometric light curve. As indicated by the right-hand panel of Fig. 4, SN 2016iyc lies towards the fainter limit of SNe IIB in the comparison sample. It is also worth mentioning that the low-luminosity SNe with low ^{56}Ni yields are thought to arise from progenitors having masses near the threshold mass for producing a CCSN (Smartt et al. 2009).

Furthermore, the bolometric luminosity light curve of SN 2016iyc is also produced after considering the additional black-body corrections to the observed $BVRI$ quasibolometric light curve, by fitting a single blackbody to observed fluxes at a particular epoch and integrating the fluxes trapezoidally for a wavelength range of 100–25 000 Å using SUPERBOL. Fig. A3 shows the black-body fits to the SED of SN 2016iyc. The top panel of Fig. 5 shows the resulting quasibolometric and bolometric light curves of SN 2016iyc.

3.4 Temperature and radius evolution

From SUPERBOL, the black-body temperature (T_{BB}) and radius (R_{BB}) evolution of SN 2016iyc are also obtained. During the initial phases, the photospheric temperature is high, reaching $\sim 10\,900$ K at -10.63 d. Furthermore, the SN seems to evolve very rapidly; its

⁶<http://edd.ifa.hawaii.edu/CF3calculator/>

Table 1. The adopted total extinction values, distances, and corresponding distance moduli of a subset of SNe considered here.

SN name	$E(B - V)_{\text{tot}}$ (mag)	Adopted distance (Mpc)	Distance modulus (mag)	V_{max} (mag)	$\log(L_{BVRI})_p$ (erg s^{-1})
SN 1987A	0.16 (Bose et al. 2021)	0.05 (Bose et al. 2021)	18.44	-15.52 ± 0.02	42.555 ± 0.004
SN 1993J	0.18 (Richmond et al. 1996)	3.68 (Bose et al. 2021)	27.82	-16.97 ± 0.03	42.01 ± 0.01
SN 2003bg	0.02 (Mazzali et al. 2009)	24 (Mazzali et al. 2009)	31.90	-17.8 ± 0.2	42.31 ± 0.03
SN 2008ax	0.3 (Tsvetkov et al. 2009)	9.6 (Pastorello et al. 2008)	29.92	-16.35 ± 0.05	42.07 ± 0.03
SN 2011dh	0.035 (Sahu, Anupama & Chakradhari 2013)	8.4 (Sahu et al. 2013)	29.62	-17.06 ± 0.02	41.99 ± 0.03
SN 2011fu	0.22 (Kumar et al. 2013)	77.0 (Kumar et al. 2013)	34.46	-17.51 ± 0.03	42.426 ± 0.006
SN 2011hs	0.17 (Bufano et al. 2014)	23.44 ^a	31.85	-16.03 ± 0.03	41.74 ± 0.02
SN 2013df	0.098 (Morales-Garoffolo et al. 2015)	16.6 (Van Dyk et al. 2014)	31.1	-16.47 ± 0.05	41.87 ± 0.01
SN 2016gkg	0.017 (Bersten et al. 2018)	26.4 (Kilpatrick et al. 2017)	32.11	-17.03 ± 0.05	41.98 ± 0.02
SN 2016iyc	0.137	46.0	33.31	-15.32 ± 0.05	41.44 ± 0.01

Notes. The sources for the $BVRI$ light curves for SNe in the comparison sample are as follows. SN 1987A, Menzies et al. (1987) and Makino et al. (1987); SN 1993J, Zhang et al. (2004); SN 2003bg, Hamuy et al. (2009); SN 2008ax, Pastorello et al. (2008); SN 2011dh, Sahu et al. (2013); SN 2011fu, Kumar et al. (2013); SN 2011hs, Bufano et al. (2014); SN 2013df, Morales-Garoffolo et al. (2015). Adopted distances have been used to calculate the distance moduli. The total extinction correction and distance moduli for all the SNe in the comparison sample have been taken into account while calculating the bolometric light curves. ^aFor SN 2011hs, the distance modulus is 31.85 mag (Bufano et al. 2014), which is used to back-calculate a distance of 23.44 Mpc.

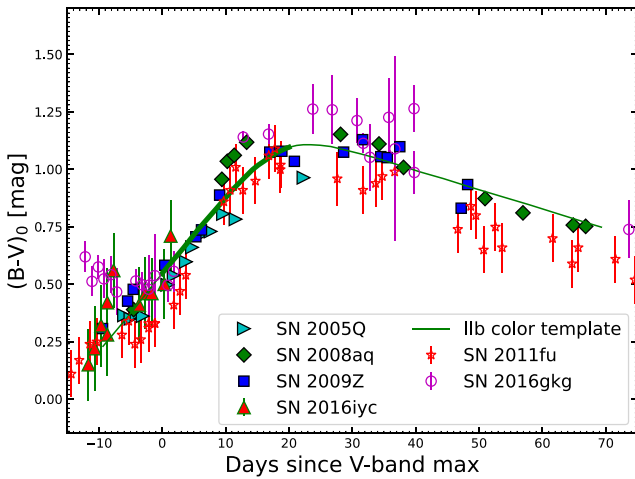


Figure 3. The total-extinction-corrected $(B - V)_0$ colour curves of SN 2016iyc, SN 2011fu, and SN 2016gkg, plotted along with other SNe I Ib. The data for SN 2005Q, SN 2008aq, and SN 2009Z were taken from Stritzinger et al. (2018), with these three SNe analysed to have negligible host-galaxy extinction. The green curve shows the template $(B - V)_0$ curve for SNe I Ib having negligible host-galaxy extinction. The thick portion of the template curve shows the 0 to +20 d period that should be considered when determining the colour excess for the reasons mentioned by Stritzinger et al. (2018).

temperature quickly drops to ~ 7600 K in only a few days around -7.7 d and then remains nearly constant (Fig. 5, second panel from top). Along with SN 2016iyc, the temperature evolution of a few more similar SNe I Ib are also shown in this panel. The black-body temperature of SN 2016iyc seems to follow the typical temperature evolution as seen in SNe I Ib.

A conventional evolution in radius is also seen. Initially, at an epoch of -10.63 d, the black-body radius is 2.64×10^{14} cm. Thereafter, the SN expands and its radius increases, reaching a maximum radius of $\sim 5.8 \times 10^{14}$ cm, beyond which the photosphere seems to recede into the SN ejecta (Fig. 5, third panel from top). Along with SN 2016iyc, the black-body radius evolution of a few more similar SNe I Ib are also shown. SN 2016iyc seems to exhibit anomalous behaviour, with its black-body radii at various epochs being the smallest among other similar SNe I Ib. This result can be attributed to the low ejecta velocity of SN 2016iyc.

4 SPECTRAL STUDIES OF SN2016iyc

In this section, we identify the signatures of various lines by modelling the only available spectrum of SN 2016iyc using SYN++ (Branch et al. 2007; Thomas, Nugent & Meza 2011). We discuss various spectral features of SN 2016iyc, and the spectrum is also compared with other similar SNe.

4.1 Spectral modelling

A single optical spectrum of SN 2016iyc was obtained on 2016 December 23 with the Kast double spectrograph (Miller & Stone 1993) mounted on the 3 m Shane telescope at Lick Observatory. Fig. 6 shows the spectral modelling of it, corresponding to a phase of -6.6 d. The individual lines corresponding to various elements and ions are also indicated for better identification of the features. The profiles of $H\alpha$ near 6563 \AA , He I near 5876 \AA , and Ca II H\&K are very nicely reproduced by SYN++ modelling. A very strong $H\alpha$ feature near 6563 \AA classifies SN 2016iyc as an SN I Ib. The observed velocities obtained using $H\alpha$, He I , and Fe II features in the spectrum are $\sim 10\,000$, ~ 6700 , and $\sim 6100 \text{ km s}^{-1}$ (respectively), while the respective velocities of these lines from SYN++ modelling are $10\,100$, 6800 , and 6100 km s^{-1} , very close to the observed ones. The parametrization velocity and photospheric velocity used to produce the SYN++ model are 6000 and 6100 km s^{-1} , respectively. Also, a photospheric temperature of 6300 K is employed to produce the model spectrum.

4.2 Spectral comparison

Fig. 7 shows a comparison of the normalized spectrum of SN 2016iyc with other well-studied SNe I Ib. The top plot displays the comparison with the spectra of SN 1993J at $+2.3$ d and -7.0 d; we see that the spectral features of SN 2016iyc closely resemble those of SN 1993J spectra. In the second panel from the top, the spectrum of SN 2016iyc is compared with spectra of SN 2011fu at $+3.4$ and -7.0 d; the match is close, except for the $H\alpha$ feature where the spectra of SN 2011fu are slightly off. The third panel from the top shows the spectral comparison of SN 2016iyc with spectra of SN 2013df at epochs of $+2.7$ and -11.0 d, revealing a good match with the -11.0 d spectrum. The progenitor of SN 2013df is also thought to be arising from the lower mass end. In the bottom panel, the spectrum of SN 2016iyc is compared with spectra of SN 2016gkg at epochs of -0.7 d and

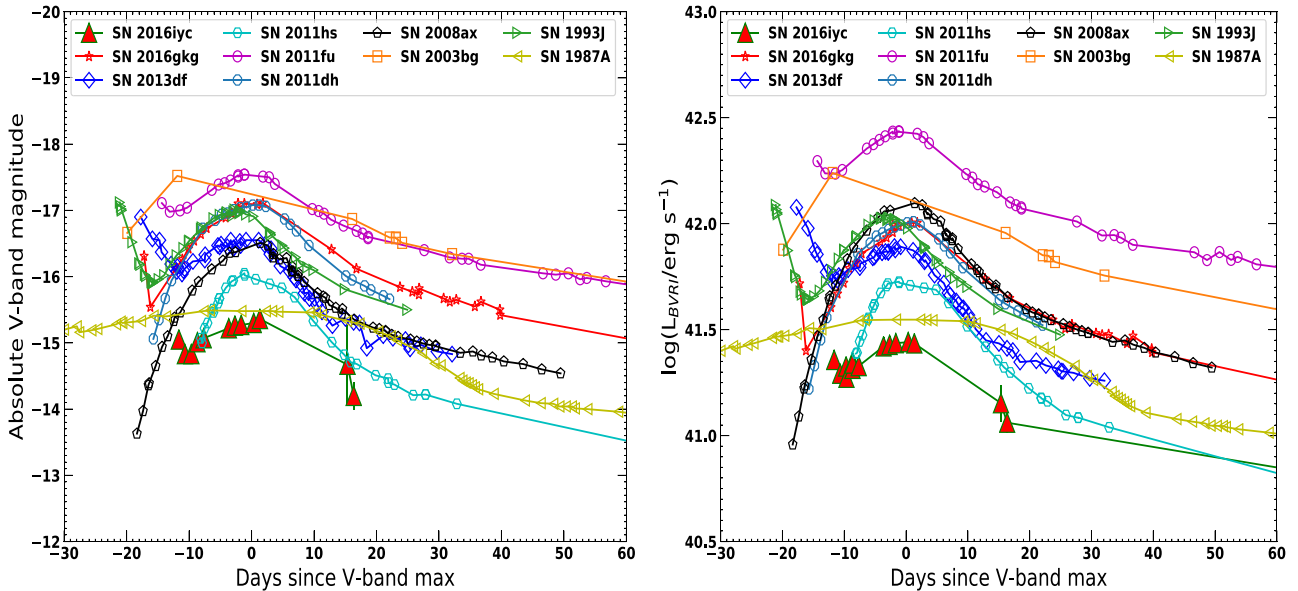


Figure 4. *Left:* Comparison of the absolute V-band light curves of SN 2016iyc and SN 2016gkg with other well-studied SNe IIB (the peculiar Type II SN 1987A, included in the sample because of its low luminosity). *Right:* Comparison of the quasibolometric light curves of SN 2016iyc and SN 2016gkg with other well-studied SNe IIB obtained by integrating the fluxes over the BVRI bands. SN 2016iyc lies towards the faint end of SNe IIB. The total extinction correction and distance moduli for all the SNe in the comparison sample have been taken into account while calculating these light curves.

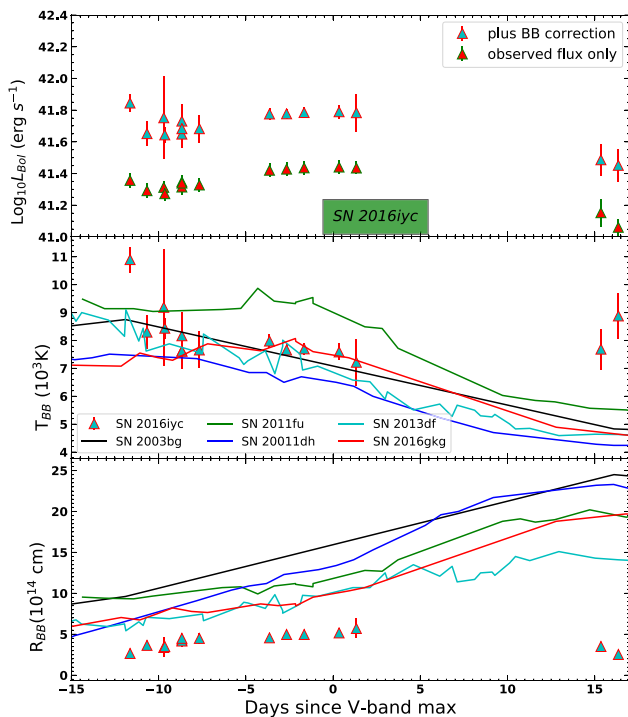


Figure 5. The top panel shows the bolometric and quasibolometric light curves of SN 2016iyc. The luminosity corresponding to the late upper limits on BVRI are shown later. The second and third panels from the top, respectively, display the black-body temperature and radius evolutions of SN 2016iyc.

+16 d. The -0.7 d spectrum of SN 2016gkg resembles the spectrum of SN 2016iyc towards the bluer side, while features in the redder part of the spectrum are slightly off. The +16 d spectrum of SN 2016gkg does not show a good resemblance with the spectrum of SN 2016iyc.

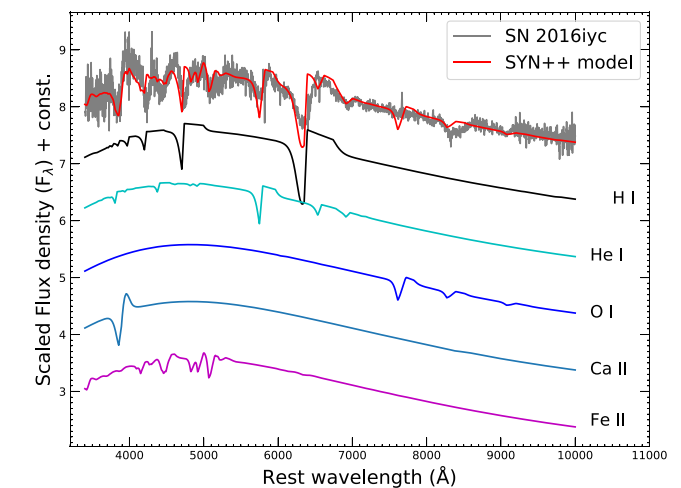


Figure 6. SYN++ modelling of the spectrum of SN 2016iyc at a phase of -6.6 d. The effects of various elements present in the SN ejecta and contributing to the spectrum are also displayed individually.

From Fig. 7, we conclude that the spectrum of SN 2016iyc shows close resemblance with the spectra of other well-studied SNe IIB, thereby providing good evidence for the classification of SN 2016iyc as an SN IIB.

5 POSSIBLE PROGENITOR MODELLING AND THE RESULTS OF SYNTHETIC EXPLOSIONS FOR SN 2016iyc

To constrain the physical properties of the possible progenitor of SN 2016iyc, we attempted several progenitor models. Following the available literature, SN 2016iyc lies near the faint limit (see Table 1), with M_{ej} also close to the lowest limit (Table 2). As mentioned earlier, low-luminosity SNe with low ⁵⁶Ni production are thought

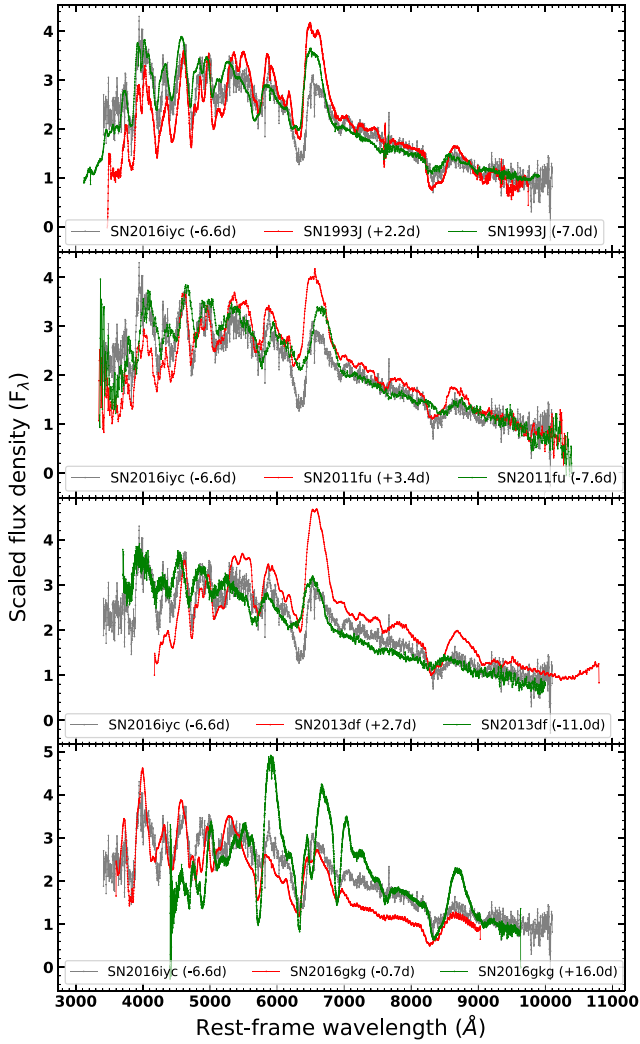


Figure 7. Comparison of the -6.6 d spectrum of SN 2016iyc with spectra of other well-studied SNe IIB, including SN 1993J, SN 2011fu, SN 2013df, and SN 2016gkg.

Table 2. Ejecta masses of various SNe IIB and SN 2016iyc.

SN name	M_{ej}	Source
SN 1993J	1.9–3.5	Young, Baron & Branch (1995)
SN 2003bg	4	Mazzali et al. (2009)
SN 2008ax	2–5	Taubenberger et al. (2011)
SN 2011dh	1.8–2.5	Bersten et al. (2012)
SN 2011fu	3.5	Morales-Garoffolo et al. (2015)
SN 2011hs	1.8	Bufano et al. (2014)
SN 2013df	0.8–1.4	Morales-Garoffolo et al. (2014)
SN 2016gkg	3.4	Bersten et al. (2018)
SN 2016iyc	1.2	Zheng et al. (2022)

to arise from progenitors having masses near the threshold mass for producing CCSNe (Smartt 2009). With low M_{ej} among typical SNe IIB and having intrinsically low luminosity, we started with the nearly lowest possible ZAMS progenitor mass of $9 M_{\odot}$ for a Type IIB SN. Starting from the pre-main sequence, the model could be evolved up to the onset of core collapse. But the $9 M_{\odot}$ model at pre-SN phase in our simulation is very compact, having a radius of only $0.14 R_{\odot}$. Such a compact progenitor cannot generate the generic extended-

SBO feature of typical SNe IIB. Furthermore, no direct observational signatures have been found for an SN IIB arising from a progenitor having ZAMS mass $\leq 11 M_{\odot}$, so we do not make any further attempt to model progenitors having masses $\leq 11 M_{\odot}$. Thus, we select models having ZAMS masses of 12, 13, and $14 M_{\odot}$, and evolve them up to the onset of core collapse. Such models originating from the lower limits of progenitor mass systems lack sufficiently strong winds to suffer much stripping; thus, the models are artificially stripped to mimic the effect of a binary companion. A brief description of our models is provided below.

We first evolve the non-rotating 9, 12, 13, and $14 M_{\odot}$ ZAMS stars until the onset of core collapse, using the one-dimensional stellar evolution code MESA (Paxton et al. 2011, 2013, 2015, 2018).

For the $9 M_{\odot}$ model, $\alpha_{MLT} = 2.0$ is used throughout the evolution, except for the phase when the model evolves to reach the beginning of core-Si burning (i.e. in the `inlist_to_si_burn` file), where $\alpha_{MLT} = 0.01$ is used. At this phase, the evolution of the models is extremely sensitive to this α_{MLT} , since even a slight change (say, 0.02) results in the failure of the beginning of core-Si burning. Although $\alpha_{MLT} = 0.01$ seems to be very low, this is required for the successful evolution of considered models through the last phases of their evolution. Furthermore, as mentioned by Joyce & Chaboyer (2018), α_{MLT} is neither a physical constant nor a computational one; it is rather a free parameter, so its value must be determined on an individual basis in each stellar evolution code. Thus, as $\alpha_{MLT} = 0.01$ is helpful for evolving the models beyond the beginning of core-Si burning, it is acceptable. For the 12, 13, and $14 M_{\odot}$ models, $\alpha_{MLT} = 3.0$ is used throughout the evolution.

Convection is modelled using the mixing theory of Henyey, Vardya & Bodenheimer (1965), adopting the Ledoux criterion. Semi-convection is modelled following Langer, El Eid & Fricke (1985) with an efficiency parameter of $\alpha_{sc} = 0.01$. For the thermohaline mixing, we follow Kippenhahn, Ruschenplatt & Thomas (1980), and set the efficiency parameter as $\alpha_{th} = 2.0$. We model the convective overshoot with the diffusive approach of Herwig (2000), with $f = 0.001$ and $f_0 = 0.007$ for all the convective cores and shells. We use the ‘Dutch’ scheme for the stellar wind, with a scaling factor of 1.0. The ‘Dutch’ wind scheme in MESA combines results from several papers. Specifically, when $T_{eff} > 10^4$ K and the surface mass fraction of H is greater than 0.4, the results of Vink, de Koter & Lamers (2001) are used, and when $T_{eff} > 10^4$ K and the surface mass fraction of H is less than 0.4, the results of Nugis & Lamers (2000) are used. In the case when $T_{eff} < 10^4$ K, the de Jager, Nieuwenhuijzen & van der Hucht (1988) wind scheme is used.

SNe IIB have been considered to originate from massive stars that have retained a significant amount of their hydrogen envelope. We have adopted a mass-loss rate of $\dot{M} \gtrsim 10^{-4} M_{\odot} \text{ yr}^{-1}$ to artificially strip the models until the final M_H reaches in range of $(0.013\text{--}0.055) M_{\odot}$. Such extensive mass-loss rates are supported by the studies performed by Ouchi & Maeda (2017), where they mention that the binary scenario for the progenitors of SNe IIB leads to such high mass-loss rates. Furthermore, van Loon et al. (2005) have also reported extensive mass-loss rates reaching $\dot{M} = 10^{-4} M_{\odot} \text{ yr}^{-1}$, solely by a single stellar wind.

Once the models have stripped off upto the specified limit of the H envelope, we switch off the artificial mass loss and further evolve the models until the onset of core collapse. Corresponding to various ZAMS masses, the amount of remaining H varies. Massive progenitors with a similar rate of stripping as less-massive progenitors will retain a larger amount of H. In our simulations, the specified limit on H mass depends primarily on (a) the model’s ability to evolve up to the stage of core collapse by retaining the specified

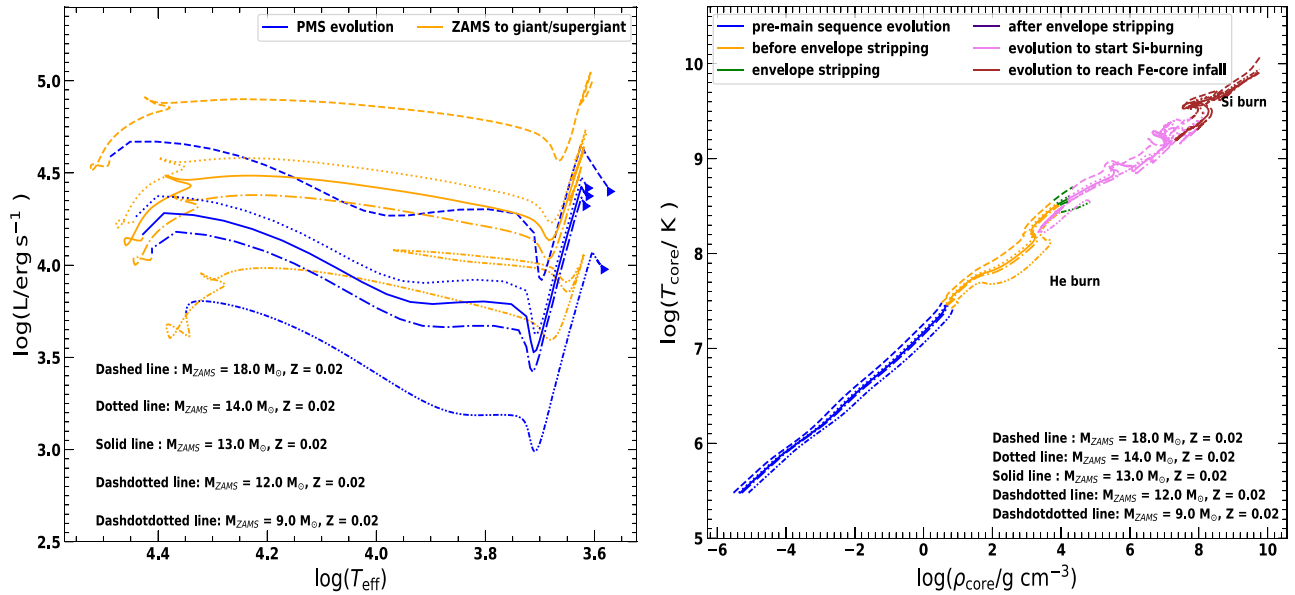


Figure 8. *Left:* The evolution of 9.0 M_{\odot} , 12 M_{\odot} , 13 M_{\odot} , 14 M_{\odot} , and 18.0 M_{\odot} ZAMS progenitors with $Z = 0.02$ on the HR diagram. The models begin evolution on the pre-main sequence (blue curve), then reach the main sequence and evolve until they become giants/supergiants with being ready to strip their outer envelopes (orange curve). *Right:* The variation of core temperature with core density as the models evolves through various phases on the HR diagram. The core-He and core-Si burning phases are marked. The onset of Fe-core infall in the models is marked by the core temperatures and core densities reaching above 10^{10} K and 10^{10} g cm^{-3} , respectively.

Table 3. MESA model and STELLA/SNEC explosion parameters of various models for SN 2016iyc.

Model name	M_{ZAMS} (M_{\odot})	Z	M_{H}^a (M_{\odot})	R_0^b (R_{\odot})	f_{ov}^c	M_{f}^d (M_{\odot})	M_{ci}^e (M_{\odot})	M_{cf}^f (M_{\odot})	M_{ej}^g (M_{\odot})	M_{Ni}^h (M_{\odot})	E_{exp}^i (10^{51} erg)
M9_Z0.0200_Mni0.034_E0.56	9.0	0.0200	0.013	0.14	0.007	2.17	1.4	1.4	0.77	0.034	0.56
M12_Z0.0215_Mni0.02_E0.33	12.0	0.0215	0.035	596	0.007	3.96	1.54	1.54	2.42	0.02	0.33
M12_Z0.0185_Mni0.03_E0.35	12.0	0.0185	0.055	315	0.007	3.49	1.46	1.46	2.03	0.03	0.35
M12_Z0.0200_Mni0.025_E0.35	12.0	0.0200	0.05	300	0.007	3.45	1.52	1.52	1.93	0.025	0.35
M12_Z0.0200_Mni0.09_E0.35	12.0	0.0200	0.05	300	0.007	3.45	1.52	1.52	1.93	0.09	0.35
M13_Z0.0200_Mni0.024_E0.28	13.0	0.0200	0.04	204	0.007	3.79	1.64	1.90	1.88	0.024	0.28
M13_Z0.0200_Mni0.01_E0.32	13.0	0.0200	0.04	204	0.007	3.79	1.64	1.64	2.15	0.01	0.32
M13_Z0.0185_Mni0.02_E0.35	13.0	0.0185	0.06	318	0.007	3.92	1.53	1.56	2.36	0.02	0.35
M13_Z0.0215_Mni0.03_E0.40	13.0	0.0215	0.015	10	0.007	3.81	1.61	1.62	2.19	0.03	0.40
M14_Z0.0200_Mni0.03_E0.50	14.0	0.0200	0.03	55	0.007	4.23	1.54	1.54	2.69	0.03	0.50

^aAmount of hydrogen retained after stripping. ^bPre-SN progenitor radius. ^cOvershoot parameter. ^dFinal mass of pre-SN model. ^eInitial mass of the central remnant. ^fFinal mass of the central remnant. ^gEjecta mass. ^hNickel mass. ⁱExplosion energy.

amount of H (also, there is a limit on stripping), and (b) the radius of the pre-SN progenitor. If we need a compact progenitor, the amount of retained H is less, and if pre-SN progenitors are required to have extended envelopes, the amount of retained H is more.

The evolution of the models using MESA takes place in various steps. The models start to evolve on the pre-main sequence and reach the main sequence. The arrival of the models on the main sequence is marked when the ratio of the luminosity due to nuclear reactions and the total luminosity of the models is 0.8. Later, the models further evolve on the main sequence, becoming giants or supergiants. As a next step, artificial stripping of the models is performed, after which they are allowed to settle down. Once the stripping of the models reaches the specified H-envelope mass limit and the models have settled down, they further evolve until the ignition of Si burning in their core. Once the Si burning has started in the core, the models begin to develop inert iron (^{56}Fe) cores responsible for their cores to collapse.

The evolution of such models having ZAMS masses of 9, 12, 13, and 14 M_{\odot} with metallicity $Z = 0.0200$ on the Hertzsprung–Russell (HR) diagram is illustrated in the left-hand panel of Fig. 8. We simulated a total of nine models covering progenitor masses of 9–14 M_{\odot} and also covering subsolar to supersolar metallicity wherever necessary. The pre-explosion properties using MESA and explosion properties using STELLA/SNEC are listed in Table 3. The models have been so named that they include informations of ZAMS mass, metallicity, M_{Ni} , and E_{exp} . Thus, the model M9_Z0.0200_Mni0.034_E0.56 has a ZAMS mass of 9 M_{\odot} , $Z = 0.0200$, $M_{\text{Ni}} = 0.034 M_{\odot}$, and $E_{\text{exp}} = 0.56 \times 10^{51}$ erg.

The right-hand panel of Fig. 8 shows the variation of core temperature (T_{core}) with core density (ρ_{core}) as the models evolve through various phases on the HR diagram. The core-He and core-Si burning phases are marked. The onset of core collapse is marked by T_{core} and ρ_{core} reaching above $\sim 10^{10}$ K and 10^{10} g cm^{-3} , respectively. The left-hand panel of Fig. 9 shows the mass fractions of various

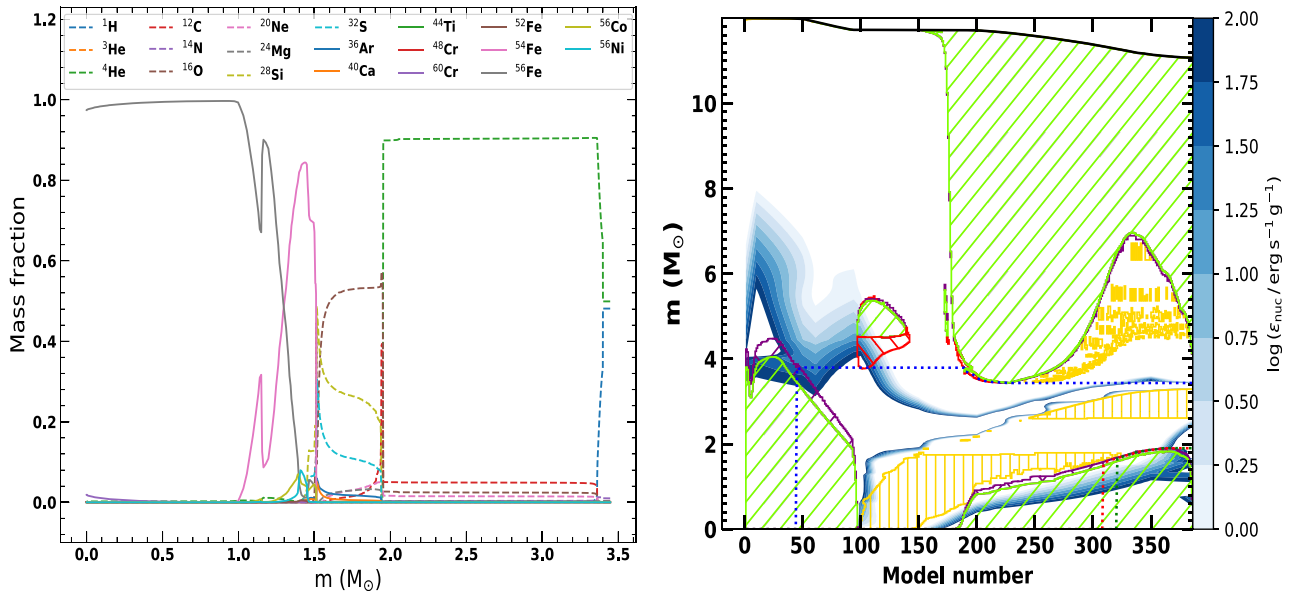


Figure 9. *Left:* The mass fractions of a few key elements when the $12 M_{\odot}$ ZAMS progenitor model with $Z = 0.02$ has just reached the stage of Fe-core infall. Notice the very high mass fraction of ^{56}Fe in the core compared to other species. *Right:* The Kippenhahn diagram of the same model for a period from the beginning of main-sequence evolution to the stage when the model is ready to be stripped.

species present when the $12 M_{\odot}$ model (with $Z = 0.0200$) has achieved Fe-core infall. The core is composed mainly of ^{56}Fe with negligible fractions of other species. Significant fractions of heavier metals are seen towards the surface of the pre-explosion progenitor. The right-hand panel of Fig. 9 shows the Kippenhahn diagram for the $12 M_{\odot}$ model (with $Z = 0.0200$) for a period from the beginning of main-sequence evolution to the stage when the model is ready to begin envelope stripping. In this figure, the convective regions are marked by the hatchings with the logarithm of the specific nuclear energy generation rate (ϵ_{nuc}) inside the stellar interiors marked with the blue colours. The dark-yellow regions indicate the stellar interior where the thermohaline mixing is going on.

Using the progenitor models on the verge of core collapse obtained through MESA, we carried out radiation hydrodynamic calculations to simulate the synthetic explosions. For this purpose, we used STELLA (Blinnikov et al. 1998, 2000; Branch et al. 2006) and SNEC (Morozova et al. 2015). STELLA solves the radiative transfer equations in the intensity momentum approximation in each frequency bin, while SNEC is a one-dimensional Lagrangian hydrodynamic code that solves the radiation energy transport equations in the flux-limited diffusion approximation. STELLA and SNEC, both generate the bolometric light curve and the photospheric velocity evolution of the SN, along with a few other observed parameters. The radioactive decay of ^{56}Ni to ^{56}Co is considered to be one of the prominent mechanisms for powering the primary peak of SNe IIB. Both of these codes incorporate this model by default. Thus in this section, we model the entire bolometric light curve of the SN 2016iyc assuming this powering mechanism. Here, we provide the set-up of the explosions to incorporate the Ni–Co decay model. The set-ups for simulating the synthetic explosion using SNEC and STELLA closely follow Ouchi & Maeda (2019) and Aryan et al. (2021), respectively. Here, we briefly summarize the important parameters and modifications made to Ouchi & Maeda (2019) and Aryan et al. (2021).

We simulate the synthetic explosions of the $9 M_{\odot}$ model using SNEC. First, the innermost $1.4 M_{\odot}$ is excised before the explosion,

assuming that the model collapses to form neutron stars. The number of grid cells is set to be 1000 so that the light curves and photospheric velocities of the SNe from synthetic explosions are well converged in the time domain of interest.

For the M9_Z0.0200_Mni0.034_E0.56 model, the synthetic explosion is carried out using SNEC. The explosion is simulated as a `Thermal_Bomb` by adding 0.56×10^{51} erg of energy in the inner $0.1 M_{\odot}$ of the model for a duration of 0.1 s. SNEC does not include a nuclear-reaction network, so the amount of ^{56}Ni is set by hand. A total of $0.034 M_{\odot}$ of ^{56}Ni is distributed from the inner boundary up to the mass coordinate $m(r) = 2.0 M_{\odot}$.

For the models having ZAMS masses of 12, 13, and $14 M_{\odot}$, we used STELLA to simulate the synthetic explosions. The pre-SN model masses from $12 M_{\odot}$ models lie in the range of $(3.45\text{--}3.96) M_{\odot}$, while from $13 M_{\odot}$ models, the pre-SN model masses lie in the range of $3.79\text{--}3.81 M_{\odot}$. Furthermore, the $14 M_{\odot}$ model has a pre-SN mass of $4.23 M_{\odot}$ and is thus prone to produce a much higher M_{ej} than required for SN 2016iyc. For producing the synthetic explosions, the hydrodynamic simulations are performed using `Thermal_Bomb`-type explosion. Various explosion parameters including the ejecta masses, synthesized nickel masses, and explosion energies corresponding to different models are presented in Table 3.

The results of the hydrodynamic simulations are shown in Fig. 10. The left-hand panel of Fig. 10 shows the comparison of the SNEC- and STELLA-calculated bolometric light curves with the observed bolometric light curve (see Section 3.3 for details on bolometric light curves) produced by fitting black bodies to the SEDs and integrating the fluxes over the wavelength range of $100\text{--}25\,000 \text{ \AA}$, while the right-hand panel shows the comparison of the corresponding photospheric velocities with the photospheric velocity obtained using the only available spectrum indicated by the Fe II line velocity. The M9_Z0.0200_Mni_0.034_E0.56 model could match the observed stretch factor and peak of the bolometric light curve, but it fails to reproduce the early extended SBO feature. The failure in producing the generic extended-SBO feature could be associated

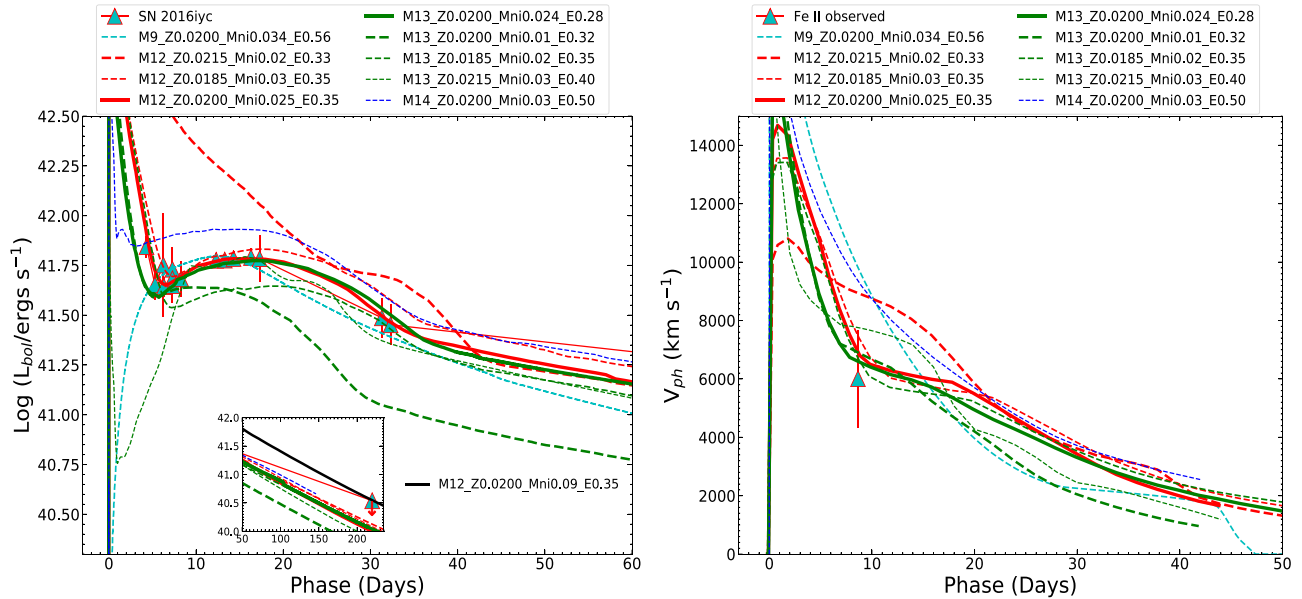


Figure 10. The results of the synthetic explosions produced using STELLA/SNEC by assuming $9 M_{\odot}$, $12 M_{\odot}$, $13 M_{\odot}$, and $14 M_{\odot}$ ZAMS stars as the possible progenitors for SN 2016iyc. *Left:* The bolometric luminosity light curves corresponding to different models having different metallicities, explosion energies, and nickel masses compared with the observed bolometric light curve of SN 2016iyc. *Right:* The corresponding photospheric velocity evolution comparison. In both the panels, the ‘Phase’ is (approximate) days since the explosion. Following Zheng et al. (2022), the adopted phase of explosion is $-4.64^{+0.67}_{-0.76}$ since first detection that corresponds to MJD 57736.47 $^{+0.67}_{-0.76}$. The velocities produced by the models are well within the error bar of the observed photospheric velocities indicated by the Fe II line velocity.

with the compactness of the pre-SN model having a radius of only $0.14 R_{\odot}$.

Moreover, all of the remaining models generate the generic extended-SBO feature, but only the M12_Z0.0200_Mni0.025_E0.35 could generate the extended-SBO and overall bolometric light curve that could match with actual bolometric light curve of SN 2016iyc. Another model that could nearly match the SN 2016iyc bolometric light curve is M13_Z0.0200_Mni0.024_E0.28. The remaining models deviate largely from the observed bolometric light curve of SN 2016iyc (the left-hand panel of Fig. 10). From the right-hand panel of Fig. 10, we find that the photospheric velocity evolution generated by the models, M13_Z0.0200_Mni0.01_E0.25 and M12_Z0.0200_Mni0.025_E0.35 pass closely to the observed line velocity from Fe II which is a good indicator of observed photospheric velocity.

We also have an upper limit on the bolometric luminosity of SN 2016iyc at a phase nearly 220 d since explosion. To produce the luminosity at that epoch, the model M12_Z0.0200_Mni0.025_E0.35 requires $M_{\text{Ni}} = 0.09 M_{\odot}$ (inset plot in the left-hand panel of Fig. 10; M12_Z0.0200_Mni0.09_E0.35 is the corresponding model), serving as an upper limit on the synthesized nickel in SN 2016iyc.

Anderson (2019) has estimated a median value of $0.102 M_{\odot}$ for the nickel mass by considering 27 SNe Iib. Moreover, Afsariardchi et al. (2021) have also estimated the Ni mass for eight SNe Iib and found that except for SN 1996cb ($M_{\text{Ni}} = 0.04 \pm 0.01 M_{\odot}$) and SN 2016gkg ($M_{\text{Ni}} = 0.09 \pm 0.02 M_{\odot}$), each SN Iib has higher M_{Ni} than $0.09 M_{\odot}$. These comparisons show that SN 2016iyc definitely suffered low nickel production. Thus, the one-dimensional stellar evolution of various models along with the hydrodynamic simulations of their explosions suggest that a ZAMS progenitor having mass in the range of $12\text{--}13 M_{\odot}$ with M_{ej} in the range of $1.89\text{--}1.93 M_{\odot}$, $M_{\text{Ni}} < 0.09 M_{\odot}$, and $E_{\text{exp}} = (0.28\text{--}0.35) \times 10^{51}$ erg could be the possible progenitor of SN 2016iyc.

Recent studies suggest the masses of possible progenitors of Type Iib CCSNe to be usually higher than $9 M_{\odot}$, lying in the range of $10\text{--}18 M_{\odot}$ (Van Dyk et al. 2013; Folatelli et al. 2014; Smartt 2015). However, there has been no direct observational evidence of an SN Iib arising from a ZAMS progenitor of $\lesssim 12 M_{\odot}$. The present analysis indicates that SN 2016iyc arises from the lower mass end of the SN Iib progenitor channel. As part of our study, we also performed the one-dimensional stellar evolutions of the possible progenitors of SN 2016gkg and SN 2011fu, and we simulated their hydrodynamic explosions in the next section to cover the range of faintest (SN 2016iyc), intermediate (SN 2016gkg), and highest (SN 2011fu) luminosity SNe in the comparison sample.

6 STELLAR MODELLING AND SYNTHETIC EXPLOSIONS FOR SN 2016gkg AND SN 2011fu

In this section, we perform hydrodynamic simulations of explosions from the possible progenitors of an intermediate-luminosity SN 2016gkg and the most-luminous SN 2011fu in the comparison sample to cover the higher end of the progenitor masses of SNe Iib. After modelling their progenitors using MESA, we simulate the synthetic explosions using SNEC and match the SNEC produced bolometric light curves with the observed ones.

To construct the bolometric light curve of SN 2016gkg, we used the recalibrated *BVRI* KAIT data along with the data from the 3.6 m DOT at two epochs and incorporated SUPERBOL. The photometric data of SN 2016gkg in this work are presented in Table A2. Previously, Bersten et al. (2018) also used KAIT data calibrated from an older KAIT reduction pipeline. Fig. A4 shows the comparison between the KAIT data used by Bersten et al. (2018) and the recalibrated KAIT data. To construct the bolometric light curve of SN 2011fu, we make use of SUPERBOL as we did in earlier sections by incorporating the *BVRI* data from Kumar et al. (2013).

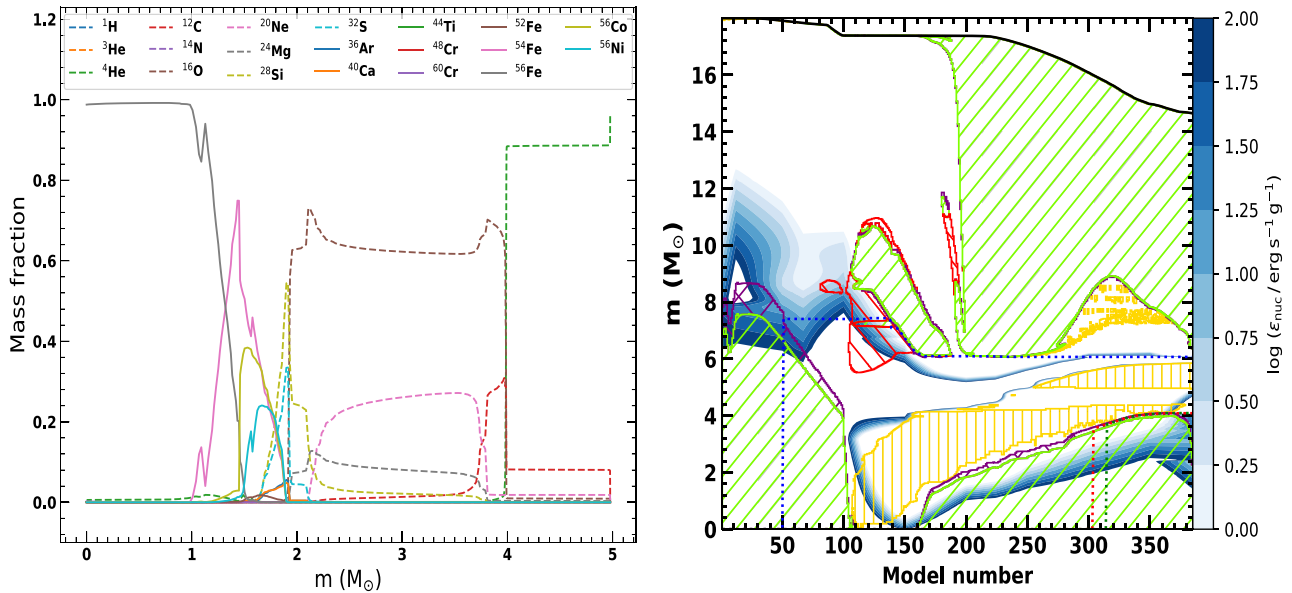


Figure 11. *Left:* The mass fractions of a few key elements when the $18 M_{\odot}$ ZAMS progenitor model with $Z = 0.02$ has just reached the stage of Fe-core infall. The mass fraction of ^{56}Fe in the centre is much higher compared to other species. *Right:* The Kippenhahn diagram of the model for a period from the beginning of main-sequence evolution to the stage when the model is ready to be stripped.

To model the possible progenitor of SN 2016gkg, we closely follow the HE5 model from Bersten et al. (2018). Also, Morales-Garoffolo et al. (2015) suggests a nearly similar model for the possible progenitor of SN 2011fu. An $18 M_{\odot}$ ZAMS progenitor mass is employed for both SNe. The modelling and explosion parameters are listed in Table A3. Starting from the ZAMS, the model is evolved up to the stage where the core starts to collapse. The evolution of the model on the HR diagram is shown in the left-hand panel of Fig. 8. Various physical processes during the evolution on the HR diagram have been indicated. Also, the right-hand panel displays the variation of T_{core} with ρ_{core} . It is indicated that during the last evolutionary phases, the core density and temperatures have reached over $10^{10} \text{ g cm}^{-3}$ and 10^{10} K , respectively. Such high core density and temperatures mark the onset of core collapse. The left-hand panel of Fig. 11 shows the mass fractions of various elements at the stage when the model has just reached the stage of Fe-core infall. As another piece of evidence for the onset of core collapse, we can see that the core is mainly composed of inert ^{56}Fe . The right-hand panel of Fig. 11 shows the Kippenhahn diagram of the model for a period from the beginning of main-sequence evolution to the stage when the model is ready to be stripped.

Models He5_A and He5_B are used for SN 2016gkg and SN 2011fu, respectively. Although the parameters including the ZAMS mass, metallicity, rotation, and overshoot parameter are same for these two models, different explosion parameters are employed using SNEC to simulate the synthetic explosions.

The left-hand panel of Fig. 12 illustrates the comparison of our hydrodynamic simulation of synthetic explosions for SN 2016gkg with the results of Bersten et al. (2018). The difference between the bolometric light curve from Bersten et al. (2018) and calculated using KAIT revised photometry are within the error bars. Our model could explain the bolometric light curve of SN 2016iyc very well. Furthermore, the right-hand panel of Fig. 12 shows the comparison of the SNEC-calculated bolometric light curve with the observed quasibolometric light curve of SN 2011fu. The one-dimensional stellar modelling of possible progenitors using MESA along with

their hydrodynamic simulation of explosions using SNEC explain the observed light curves of SN 2016gkg and SN 2011fu very well. Now, we have performed the stellar modelling of the possible progenitors and the hydrodynamic explosions of SN 2016iyc, SN 2016gkg, and SN 2011fu to cover a range of faintest (SN 2016iyc), intermediate (SN 2016gkg), and highest (SN 2011fu) luminosity SNe in the comparison sample.

7 DISCUSSION

Detailed photometric and spectroscopic analyses of the low-luminosity Type IIb SN 2016iyc are performed in this work. The extinction-corrected data of SN 2016iyc are used to construct the quasibolometric and bolometric light curves using SUPERBOL. Comparisons of the absolute V -band and quasibolometric light curves of SN 2016iyc with other well-studied SNe IIb indicates that SN 2016iyc lies towards the faint limit of this subclass. Low-luminosity SNe IIb with low ^{56}Ni production are thought to arise from progenitors having masses near the threshold mass for producing a CCSN.

Our study indicates that among the comparison sample in this work, SN 2016iyc has the smallest black-body radius at any given epoch. This anomalous behaviour could be attributed to its low ejecta velocity.

Based on the low M_{ej} and the lowest intrinsic brightness among SNe in the comparison sample, 9–14 M_{\odot} ZAMS progenitors are modelled as the possible progenitor of SN 2016iyc using MESA. The results of synthetic explosions simulated using STELLA and SNEC are in good agreement with the observed ones.

The one-dimensional stellar modelling of the possible progenitor using MESA and simulations of hydrodynamic explosions using SNEC/STELLA indicate that SN 2016iyc originated from a (12–13) M_{\odot} ZAMS progenitor, near the lower end of progenitor masses for SNe IIb. The models show a range of parameters for SN 2016iyc, including $M_{\text{ej}} = (1.89\text{--}1.93) M_{\odot}$ and $E_{\text{exp}} = (0.28\text{--}0.35) \times 10^{51} \text{ erg}$. We also put an upper limit of $0.09 M_{\odot}$ on the amount of nickel

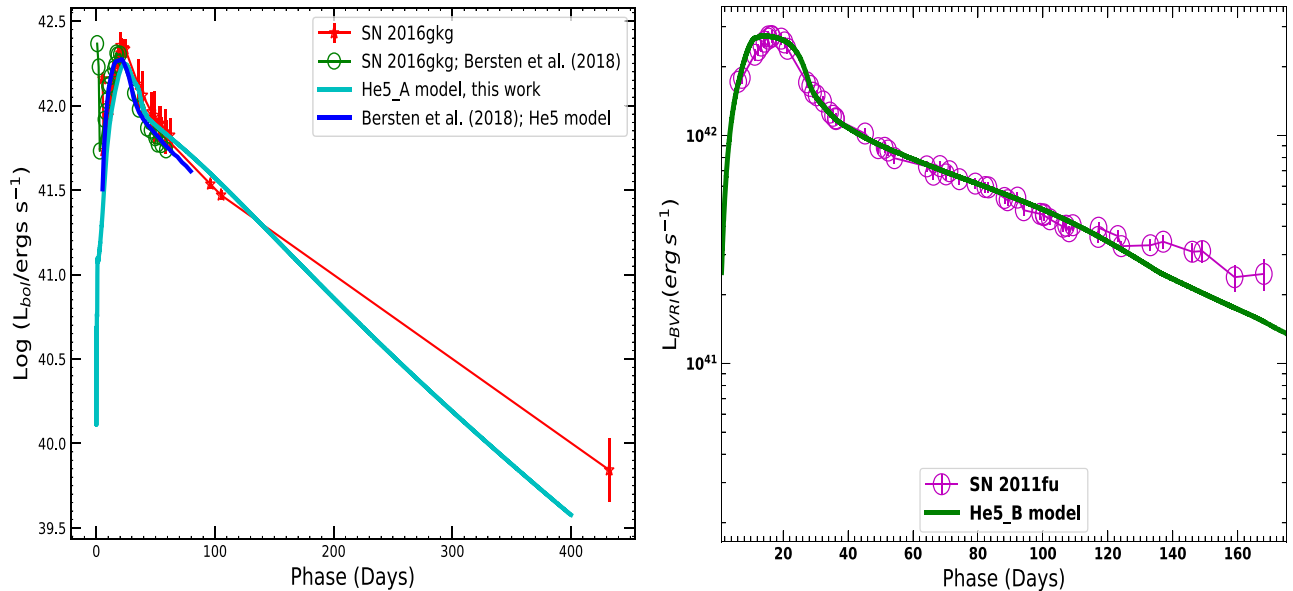


Figure 12. The results of one-dimensional stellar evolution of models using MESA and their synthetic explosion using SNEC for SN 2016gkg and SN 2011fu. *Left:* Comparison of the quasisbolometric light curve of SN 2016gkg with that obtained, using SNEC by taking into account the ^{56}Ni and ^{56}Co decay model and keeping the parameters close to those of Bersten et al. (2018). *Right:* Result of a similar analysis for SN 2011fu.

synthesized by the SN. The pre-SN radius of the progenitor of SN 2016iyc is $(204\text{--}300) R_{\odot}$.

Stellar evolution of the possible progenitors and hydrodynamic simulations of synthetic explosions of SN 2016gkg and SN 2011fu have also been performed to compare the intermediate- and high-luminosity ends among well-studied SNe IIB using MESA and SNEC. The results of stellar modelling and synthetic explosions for SN 2016iyc, SN 2016gkg, and SN 2011fu exhibit a diverse range of mass of the possible progenitors for SNe IIB.

8 CONCLUSIONS

We performed detailed photometric and spectroscopic analyses of SN 2016iyc, a Type IIB SN discovered by LOSS/KAIT. The observed photometric properties of SN 2016iyc were unique in many ways: low luminosity, low ejecta mass, and small black-body radius. Attempts to model the possible progenitor were made using the one-dimensional hydrodynamic code MESA. As a part of the present work, hydrodynamic modelling of the synthetic explosion of an intermediate-luminosity Type IIB SN 2016gkg using recalibrated KAIT data and late-time data from the 3.6 m DOT, along with an optically very luminous Type IIB SN 2011fu, were also performed. The main results based on the present analysis are as follows:

(i) Based on the low value of M_{ej} , ZAMS stars having masses of $9\text{--}14 M_{\odot}$ were adopted to model the possible progenitor of SN 2016iyc using MESA. The results of synthetic explosions simulated using SNEC and STELLA were in good agreement with observed properties for ZAMS progenitor masses of $12\text{--}13 M_{\odot}$ having a pre-SN radius of $(204\text{--}300) R_{\odot}$. Thus, SN 2016iyc likely had a progenitor arising from the lower end of the progenitor mass channel of an SN IIB.

(ii) We concluded that the overall detailed hydrodynamic simulations of the explosions from various models showed a range of parameters for SN 2016iyc, including an M_{ej} of $(1.89\text{--}1.93) M_{\odot}$, an E_{exp} of $(0.28\text{--}0.35) \times 10^{51}$ erg, and an upper limit of $<0.09 M_{\odot}$ on the amount of nickel synthesized by SN 2016iyc.

(iii) Finally, one-dimensional stellar evolution models of possible progenitors and the hydrodynamic explosions of SN 2016gkg and SN 2011fu were also performed to compare intermediate- and high-luminosity examples among well-studied SNe IIB. The results for SN 2016iyc, SN 2016gkg, and SN 2011fu showed a diverse range of mass $[(12.0\text{--}18.0) M_{\odot}]$ for the possible progenitors of SNe IIB considered in this work. Discovery of more such events through survey projects in the near future should provide additional data with which to establish the lower mass limits of such explosions.

ACKNOWLEDGEMENTS

We thank the anonymous referee for providing very useful and constructive comments that helped to improve the manuscript significantly. AA acknowledges funds and assistance provided by the Council of Scientific & Industrial Research (CSIR), India with the file no. 09/948(0003)/2020-EMR-I. AA, SBP, and RG also acknowledge BRICS grant DST/IMRCD/BRICS/Pilotcall/ProFCheap/2017(G). RG and SBP acknowledge the financial support of ISRO under AstroSat archival Data utilization program (DS_2B-13013(2)/1/2021-Sec.2). We sincerely acknowledge the extensive use of the High Performance Computing (HPC) facility at ARIES.

Support for AVF's supernova research group has been provided by the TABASGO Foundation, the Christopher R. Redlich Fund, the U.C. Berkeley Miller Institute for Basic Research in Science (where AVF was a Senior Miller Fellow), and numerous individual donors. Additional support was provided by NASA/HST grant GO-15166 from the Space Telescope Science Institute (STScI), which is operated by the Associated Universities for Research in Astronomy, Inc. (AURA), under NASA contract NAS 5-26555. JV is supported by the project 'Transient Astrophysical Objects' (GINOP 2.3.2-15-2016-00033) of the National Research, Development, and Innovation Office (NKFIH), Hungary, funded by the European Union. We acknowledge Prof. Keiichi Maeda for useful scientific discussions. The 'Open Supernova Catalog' is duly acknowledged here for spectroscopic data.

Lick/KAIT and its ongoing operation were made possible by donations from Sun Microsystems, Inc., the Hewlett-Packard Company, AutoScope Corporation, Lick Observatory, the U.S. National Science Foundation, the University of California, the Sylvia & Jim Katzman Foundation, and the TABASGO Foundation. Research at Lick Observatory is partially supported by a generous gift from Google. Some of the data presented herein were obtained at the W. M. Keck Observatory, which is operated as a scientific partnership among the California Institute of Technology, the University of California, and NASA; the observatory was made possible by the generous financial support of the W. M. Keck Foundation. The Lick and Keck Observatory staff provided excellent assistance with the observations.

This work makes use of observations from the Las Cumbres Observatory Global Telescope Network. The authors sincerely acknowledge M. Garcia and R. Case for performing the Nickel observations.

DATA AVAILABILITY

The photometric and spectroscopic data used in this work, as well as the `inlist` files to create the MESA models, can be made available on reasonable request to the corresponding author.

REFERENCES

- Afsariardchi N., Drout M. R., Khatami D. K., Matzner C. D., Moon D.-S., Ni Y. Q., 2021, *ApJ*, 918, 89
- Aldering G., Humphreys R. M., Richmond M. W., 1994, *AJ*, 107, 662
- Anderson J. P., 2019, *A&A*, 628, A7
- Arnett W. D., 1980, *ApJ*, 237, 541
- Arnett W. D., 1982, *ApJ*, 253, 785
- Arnett W. D., 1996, in Spergel D. N., ed., *Supernovae and Nucleosynthesis*, Princeton Series in Astrophysics. Princeton Univ. Press, Princeton, NJ
- Arnett W. D., Fu A., 1989, *ApJ*, 340, 396
- Aryan A. et al., 2021, *MNRAS*, 505, 2530
- Ben-Ami S. et al., 2015, *ApJ*, 803, 40
- Bersten M. C. et al., 2012, *ApJ*, 757, 31
- Bersten M. C. et al., 2014, *AJ*, 148, 68
- Bersten M. C. et al., 2018, *Nature*, 554, 497
- Blinnikov S. I., Eastman R., Bartunov O. S., Popolitov V. A., Woosley S. E., 1998, *ApJ*, 496, 454
- Blinnikov S., Lundqvist P., Bartunov O., Nomoto K., Iwamoto K., 2000, *ApJ*, 532, 1132
- Blinnikov S. I., Röpke F. K., Sorokina E. I., Gieseler M., Reinecke M., Travaglio C., Hillebrandt W., Stritzinger M., 2006, *A&A*, 453, 229
- Bose S. et al., 2021, *MNRAS*, 503, 3472
- Branch D., Parrent J., Troxel M. A., Casebeer D., Jeffery D. J., Baron E., Ketchum W., Hall N., 2007, *AIPC*, 924, 342
- Bufano F. et al., 2014, *MNRAS*, 439, 1807
- Cao Y. et al., 2013, *ApJ*, 775, L7
- Chatzopoulos E., Wheeler J. C., Vinko J., Horvath Z. L., Nahy A., 2013, *ApJ*, 773, 76
- Chevalier R. A., Fransson C., 1982, *ApJ*, 258, 790
- Chevalier R. A., Fransson C., 1994, *ApJ*, 420, 268
- Crockett R. M. et al., 2008, *MNRAS*, 391, L5
- de Jaeger T. et al., 2019, *MNRAS*, 490, 2799
- de Jager C., Nieuwenhuijzen H., van der Hucht K. A., 1988, *A&AS*, 72, 259
- de Kouchkovsky M. et al., 2016, *TNSTR*, 1056, 1
- Eldridge J. J., Langer N., Tout C. A., 2011, *MNRAS*, 414, 3501
- Filippenko A. V., 1982, *PASP*, 94, 715
- Filippenko A. V., 1988, *AJ*, 96, 1941
- Filippenko A. V., 1993, *IAU Circ.*, 5737
- Filippenko A. V., 1997, *ARA&A*, 35, 309
- Filippenko A. V., Matheson T., Ho L. C., 1993, *ApJ*, 481, L89
- Filippenko A. V., Li W. D., Treffers R. R., Modjaz M., 2001, *ASPC*, 246, 121
- Folatelli G. et al., 2014, *ApJ*, 793, L22
- Gaskell C. M., Cappellaro E., Dinerstein H. L., Garnett D. R., Harkness R. P., Wheeler J. C., 1986, *ApJ*, 306, L77
- Ginzberg S., Balberg S., 2012, *ApJ*, 757, 178
- Giovanelli R., Haynes M. P., 1993, *AJ*, 105, 1271
- Graziani R., Courtois H. M., Lavaux G., Hoffman Y., Tully R. B., Copin Y., Pomarède D., 2019, *MNRAS*, 488, 5438
- Groh J. H., Maynet G., Georgy C., Ekstrom S., 2013, *A&A*, 558, A131
- Hamuy M. et al., 2009, *ApJ*, 703, 1612
- Henry L., Vardya M. S., Bodenheimer P., 1965, *ApJ*, 142, 841
- Herwig F., 2000, *A&A*, 360, 952
- Jerkstrand A., Ergon M., Smartt S. J., Fransson C., Sollerman J., 2015, *A&A*, 573, A12
- Joyce M., Chaboyer B., 2018, *ApJ*, 856, 10
- Kasen D., Bildsten L., 2010, *ApJ*, 717, 245
- Kilpatrick C. D. et al., 2017, *MNRAS*, 465, 4650
- Kippenhahn R., Ruschenplatt G., Thomas H.-C., 1980, *A&A*, 91, 175
- Kourkchi E., Courtois H. M., Graziani R., Hoffman Y., Pomarède D., Shaya E. J., Tully R. B., 2020, *AJ*, 159, 67
- Kumar B. et al., 2013, *MNRAS*, 431, 308
- Kumar A. et al., 2021, *MNRAS*, 502, 1678
- Kumar A., Pandey S. B., Singh A., Yadav R. K. S., Reddy B. K., Nanjappa N., Yadav S., Srinivasan R., 2022, *JApA*, 43, 27
- Landolt A., 1992, *AJ*, 104, 340
- Langer N., El Eid M. F., Fricke K. J., 1985, *A&A*, 145, 179
- Li W. et al., 2003, *PASP*, 115, 844
- Makino F., Matthews J., Suntzeff N., Pastoriza M., Storchi-Bergmann T., 1987, *IAU Circ.*, 4336
- Maund J. R. et al., 2011, *ApJ*, 739, L37
- Mazzali P. A., Deng J., Hamuy M., Nomoto K., 2009, *ApJ*, 703, 1624
- Menzies J. W. et al., 1987, *MNRAS*, 227, 39P
- Miller J. S., Stone R. P. S., 1993, *Lick Obs. Tech. Rep. No. 66*
- Morales-Garoffolo A. et al., 2014, *MNRAS*, 445, 1647
- Morales-Garoffolo A. et al., 2015, *MNRAS*, 454, 95
- Moriya T. J., Tominaga N., Blinnikov S. I., Balkanov P. V., Sorokina E. I., 2011, *MNRAS*, 415, 199
- Moriya T. J., Liu Z.-W., Izzard R. G., 2015, *MNRAS*, 450, 3264
- Morozova V., Piro A. L., Renzo M., Ott C. D., 2015, *ApJ*, 814, 63
- Nadyozhin D. K., 1994, *ApJS*, 92, 527
- Nicholl M., 2018, *RNAAS*, 2, 230
- Nicholl M., Guillochon J., Berger E., 2017, *ApJ*, 850, 55
- Nomoto K., Suzuki T., Shigeyama T., Kumagai S., Yamaoka H., Saio H., 1993, *Nature*, 364, 507
- Nomoto K. I., Iwamoto K., Suzuki T., 1995, *Phys. Rep.*, 256, 173
- Nugis T., Lamers H. J. G. L. M., 2000, *A&A*, 360, 227
- Ouchi R., Maeda K., 2017, *ApJ*, 840, 90
- Ouchi R., Maeda K., 2019, *ApJ*, 877, 92
- Pandey S. B., Yadav R. K. S., Nanjappa N., Yadav S., Reddy B. K., Sahu S., Srinivasan R., 2018, *Bulletin de la Societe Royale des Sciences de Liege*, 87, 42
- Pandey S. B. et al., 2021, *MNRAS*, 507, 1229
- Pastorello A. et al., 2008, *MNRAS*, 389, 955
- Paxton B., Bildsten L., Dotter A., Herwig F., Lesaffre P., Timmes F., 2011, *ApJS*, 192, 3
- Paxton B. et al., 2013, *ApJS*, 208, 4
- Paxton B. et al., 2015, *ApJS*, 220, 15
- Paxton B. et al., 2018, *ApJS*, 234, 34
- Planck Collaboration XIII, 2016, *A&A*, 594, A13
- Podsiadlowski P., Joss P. C., Hsu J. J. L., 1992, *ApJ*, 391, 246
- Podsiadlowski P., Hsu J. J. L., Joss P. C., Ross R. R., 1993, *Nature*, 364, 509
- Richmond M. W., Treffers R. R., Filippenko A. V., Paik Y., 1996, *AJ*, 112, 732
- Ryder S. D., Sadler E. M., Subrahmanyan R., Weiler K. W., Panagia N., Stockdale C., 2004, *MNRAS*, 349, 1093

- Sahu D. K., Anupama G. C., Chakradhari N. K., 2013, *MNRAS*, 433, 2
 Schlafly E. F., Finkbeiner D. P., 2011, *ApJ*, 737, 103
 Schlegel E. M., 1990, *MNRAS*, 244, 269
 Silverman J. M. et al., 2012, *MNRAS*, 425, 1789
 Singh A., 2021, Astrophysics Source Code Library, recorded ascl:2106.024
 Smartt S. J., 2009, *ARA&A*, 47, 63
 Smartt S. J., 2015, *PASA*, 32, e016
 Smartt S. J., Eldridge J. J., Crockett R. M., Maund J. R., 2009, *MNRAS*, 395, 1409
 Stahl B. E. et al., 2019, *MNRAS*, 490, 3882
 Stetson P. B., 1987, *PASP*, 99, 191
 Stritzinger M. D. et al., 2018, *A&A*, 609, A135
 Taubenberger S. et al., 2011, *MNRAS*, 413, 2140
 Thomas R. C., Nugent P. E., Meza J. C., 2011, *PASP*, 123, 237
 Tonry J. L. et al., 2012, *ApJ*, 750, 99
 Tsvetkov D. Y., Volkov I. M., Baklanov P., Blinnikov S., Tuchin O., 2009, *PZ*, 29, 2
 Uomoto A., 1986, *ApJ*, 310, L35
 Van Dyk S. D., 2017, *Philos. Trans. R. Soc. A*, 375, 20160277
 Van Dyk S. D. et al., 2011, *ApJ*, 741, L28
 Van Dyk S. D. et al., 2013, *ApJ*, 772, L32
 Van Dyk S. D. et al., 2014, *AJ*, 147, 37
 van Loon J. T., Cioni M.-R. L., Zijlstra A. A., Loup C., 2005, *A&A*, 438, 273
 Viani L. S., Basu S., Ong J. M. J., Bonaca A., Chaplin W. J., 2018, *ApJ*, 858, 28
 Vink J. S., de Koter A., Lamers H. J. G. L. M., 2001, *A&A*, 369, 574
 Woosley S. E., Eastman R. G., Weaver T. A., Pinto P. A., 1994, *ApJ*, 429, 300
 Young T. R., Baron E., Branch D., 1995, *ApJ*, 449, L51
 Zhang T., Wang X., Zhou X., Li W., Ma J., Jiang Z., Li Z., 2004, *AJ*, 128, 1857
 Zheng W. et al., 2022, *MNRAS*, 512, 3195

APPENDIX: TABLES AND FIGURES

Table A1. Photometry of SN 2016iyc.

MJD	<i>B</i> (mag)	<i>V</i> (mag)	<i>R</i> (mag)	<i>C</i> (mag)	<i>I</i> (mag)	Telescope
57740.144	–	–	–	17.807 ± 0.111	–	KAIT
57741.116	18.473 ± 0.075	18.262 ± 0.074	18.081 ± 0.091	17.985 ± 0.048	17.875 ± 0.103	KAIT
57742.089	18.774 ± 0.149	18.484 ± 0.118	18.102 ± 0.147	18.057 ± 0.149	17.832 ± 0.148	KAIT
57743.109	18.875 ± 0.114	18.484 ± 0.111	18.105 ± 0.117	17.987 ± 0.135	17.949 ± 0.142	KAIT
57744.087	18.796 ± 0.139	18.451 ± 0.113	17.957 ± 0.113	17.957 ± 0.143	17.731 ± 0.126	KAIT
57744.091	18.787 ± 0.054	18.299 ± 0.050	17.933 ± 0.067	– ± –	17.656 ± 0.119	Nickel
57745.092	18.865 ± 0.129	18.237 ± 0.084	18.038 ± 0.106	17.855 ± 0.115	17.658 ± 0.114	KAIT
57749.111	18.568 ± 0.105	18.090 ± 0.081	17.728 ± 0.098	17.742 ± 0.131	17.524 ± 0.130	KAIT
57750.090	18.582 ± 0.100	18.050 ± 0.075	17.735 ± 0.080	17.693 ± 0.092	17.433 ± 0.084	KAIT
57751.095	18.567 ± 0.085	18.037 ± 0.063	17.693 ± 0.070	17.665 ± 0.055	17.439 ± 0.073	KAIT
57751.095	18.567 ± 0.085	18.037 ± 0.063	17.693 ± 0.070	17.665 ± 0.055	17.439 ± 0.073	KAIT
57753.099	18.578 ± 0.083	18.009 ± 0.061	17.679 ± 0.063	17.635 ± 0.091	17.408 ± 0.082	KAIT
57754.091	18.724 ± 0.137	17.947 ± 0.066	17.678 ± 0.067	17.653 ± 0.090	17.409 ± 0.093	KAIT
57768.107	–	18.638 ± 0.059	18.582 ± 0.395	18.570 ± 0.242	18.069 ± 0.321	KAIT
57769.105	19.295 ± 0.464	19.111 ± 0.214	18.666 ± 0.194	18.784 ± 0.282	18.466 ± 0.232	KAIT
57956.471	>21.490	>21.336	>21.542	–	>20.631	Nickel

Table A2. Revised KAIT photometry of SN 2016gkg along with 3.6 m DOT data.

MJD	<i>B</i> (mag)	<i>V</i> (mag)	<i>R</i> (mag)	<i>C</i> (mag)	<i>I</i> (mag)	Telescope
57653.315	15.949 ± 0.357	15.799 ± 0.234	15.642 ± 0.214	15.661 ± 0.069	15.518 ± 0.286	KAIT
57654.322	17.039 ± 0.079	16.569 ± 0.113	16.257 ± 0.053	16.272 ± 0.030	16.056 ± 0.068	KAIT
57658.373	16.626 ± 0.054	15.990 ± 0.038	15.696 ± 0.045	15.745 ± 0.045	15.652 ± 0.050	KAIT
57659.444	16.383 ± 0.049	15.854 ± 0.041	15.557 ± 0.053	15.630 ± 0.042	15.539 ± 0.063	KAIT
57660.444	16.282 ± 0.047	15.690 ± 0.018	15.450 ± 0.022	15.429 ± 0.083	15.401 ± 0.045	KAIT
57661.316	16.106 ± 0.066	15.566 ± 0.052	15.249 ± 0.061	15.482 ± 0.071	15.183 ± 0.079	KAIT
57662.408	16.024 ± 0.060	15.466 ± 0.053	15.213 ± 0.059	15.238 ± 0.062	15.182 ± 0.085	KAIT
57663.334	15.861 ± 0.074	15.378 ± 0.068	15.125 ± 0.162	15.145 ± 0.068	15.049 ± 0.109	KAIT
57666.368	15.748 ± 0.039	15.217 ± 0.034	15.013 ± 0.045	14.992 ± 0.033	14.887 ± 0.049	KAIT
57667.373	15.676 ± 0.037	15.162 ± 0.038	14.969 ± 0.051	14.931 ± 0.025	14.868 ± 0.050	KAIT
57668.362	15.504 ± 0.035	15.009 ± 0.012	14.838 ± 0.011	–	14.763 ± 0.013	KAIT
57668.375	15.605 ± 0.117	15.093 ± 0.060	14.916 ± 0.132	14.830 ± 0.084	14.805 ± 0.146	KAIT
57669.369	15.565 ± 0.117	15.011 ± 0.139	14.845 ± 0.128	14.758 ± 0.180	14.671 ± 0.024	KAIT
57671.420	15.536 ± 0.058	15.024 ± 0.043	14.760 ± 0.051	14.759 ± 0.063	14.621 ± 0.069	KAIT
57672.330	15.576 ± 0.048	15.003 ± 0.074	14.760 ± 0.072	14.723 ± 0.054	14.590 ± 0.090	KAIT
57683.307	16.856 ± 0.023	15.699 ± 0.016	15.187 ± 0.014	–	14.951 ± 0.014	KAIT

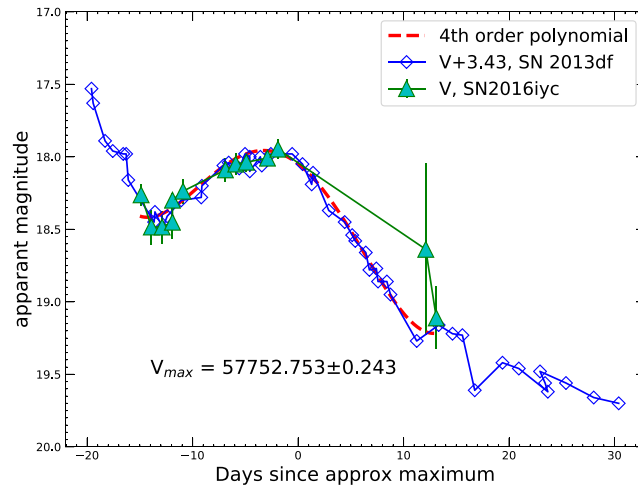
Table A2 – *continued*

MJD	<i>B</i> (mag)	<i>V</i> (mag)	<i>R</i> (mag)	<i>C</i> (mag)	<i>I</i> (mag)	Telescope
57687.298	17.165 ± 0.040	15.995 ± 0.017	15.383 ± 0.016	–	15.076 ± 0.016	KAIT
57694.279	17.545 ± 0.096	16.266 ± 0.049	15.645 ± 0.054	15.692 ± 0.053	15.226 ± 0.069	KAIT
57696.255	17.544 ± 0.021	16.302 ± 0.016	15.716 ± 0.023	–	–	3.6 m DOT
57697.300	17.560 ± 0.863	16.379 ± 0.076	15.703 ± 0.020	–	15.363 ± 0.019	KAIT
57697.350	17.562 ± 0.106	16.286 ± 0.106	15.697 ± 0.118	15.815 ± 0.016	15.372 ± 0.120	KAIT
57701.256	17.669 ± 0.081	16.440 ± 0.052	15.809 ± 0.059	15.891 ± 0.040	15.387 ± 0.059	KAIT
57702.253	17.617 ± 0.038	16.487 ± 0.018	15.833 ± 0.018	–	–	KAIT
57703.289	17.532 ± 0.108	16.463 ± 0.095	15.847 ± 0.071	15.884 ± 0.055	15.426 ± 0.053	KAIT
57706.262	17.805 ± 0.156	16.562 ± 0.071	15.894 ± 0.059	15.965 ± 0.086	15.543 ± 0.071	KAIT
57707.237	17.592 ± 0.329	16.486 ± 0.232	15.829 ± 0.186	16.023 ± 0.037	15.469 ± 0.178	KAIT
57710.259	17.893 ± 0.085	16.612 ± 0.055	16.011 ± 0.063	16.050 ± 0.046	15.535 ± 0.070	KAIT
57710.312	16.692 ± 0.084	16.689 ± 0.038	16.077 ± 0.035	–	15.617 ± 0.021	KAIT
57744.149	18.032 ± 0.109	17.277 ± 0.061	16.678 ± 0.035	–	16.143 ± 0.027	KAIT
57753.135	18.208 ± 0.039	17.371 ± 0.089	16.854 ± 0.029	–	16.282 ± 0.026	KAIT
58080.168	22.541 ± 0.258	21.751 ± 0.225	20.821 ± 0.03	–	20.137 ± 0.055	3.6 m DOT

Table A3. MESA model and SNEC explosion parameters of SN 2011fu and SN 2016gkg.

SN name	Model Name	M_{ZAMS} (M_{\odot})	Z	f_{ov}^a	M_{f}^b (M_{\odot})	M_{c}^c (M_{\odot})	M_{ej}^d (M_{\odot})	M_{Ni}^e (M_{\odot})	E_{exp}^f (10^{51} erg)
SN 2016gkg	He5_A	18.0	0.0200	0.01	5.00	1.6	3.40	0.087	1.30
SN 2011fu	He5_B	18.0	0.0200	0.01	5.00	1.5	3.50	0.140	1.25

^aOvershoot parameter. ^bFinal mass of the pre-SN model. ^cFinal mass of the central remnant ^dEjecta mass. ^eNickel mass ^fExplosion energy.

**Figure A1.** Estimation of *V*-band maximum.

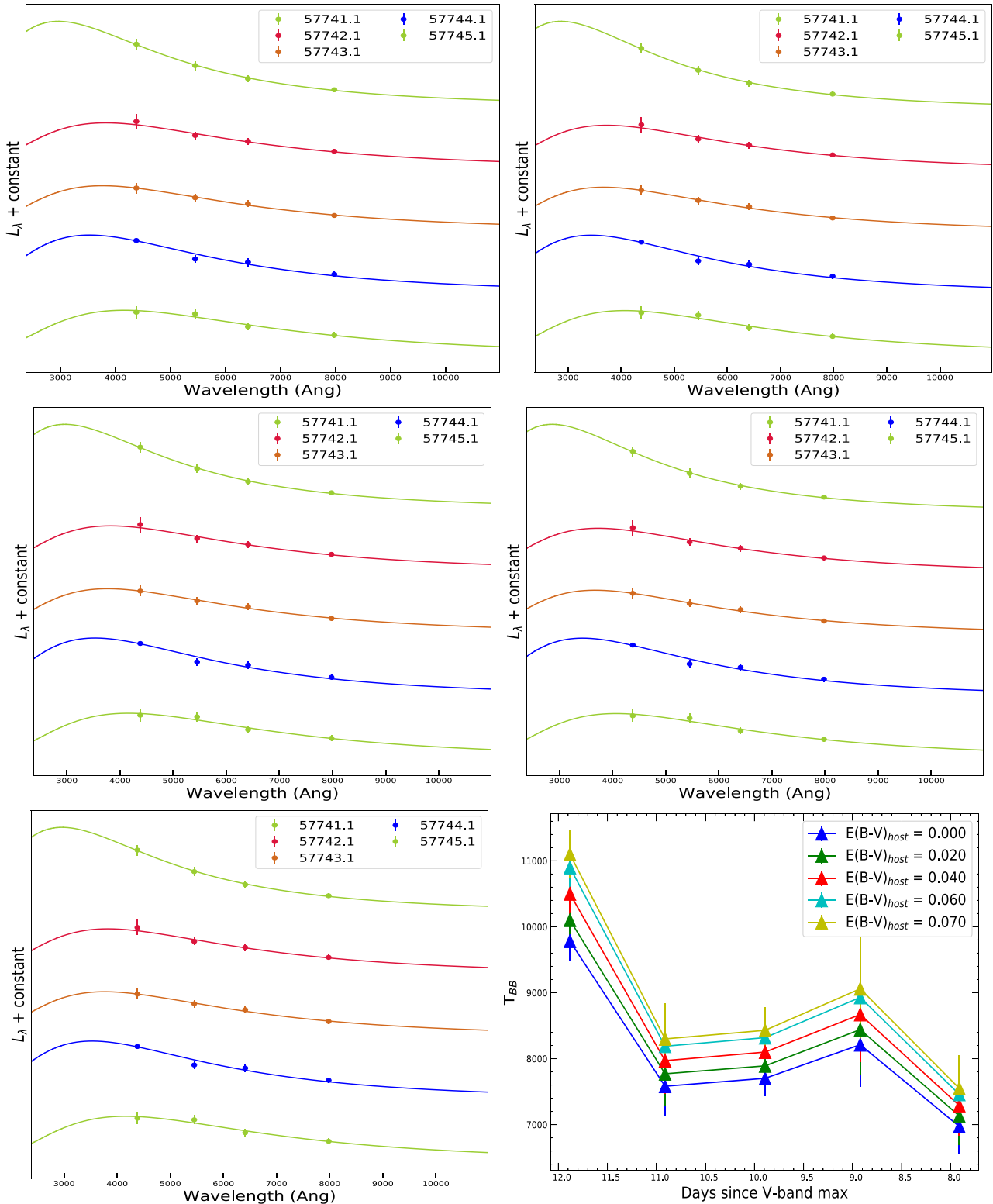


Figure A2. Fitting black-body curves to a few early epochs of SN 2016iyc by assuming different host-galaxy extinctions. The top left-hand and right-hand panels show black-body fits to a few early-epoch SEDs of SN 2016iyc corresponding to host-galaxy extinctions of 0.00 and 0.02 mag, respectively. The middle left-hand and right-hand panels show black-body fits to a few early-epoch SEDs of SN 2016iyc corresponding to host-galaxy extinctions of 0.04 and 0.06 mag, respectively. The bottom-left panel shows black-body fits to a few early-epoch SEDs of SN 2016iyc corresponding to a host-galaxy extinction of 0.07 mag, while the bottom right-hand panel shows the variation of the black-body temperature obtained using black-body fits to the SEDs corresponding to different host-galaxy extinctions.

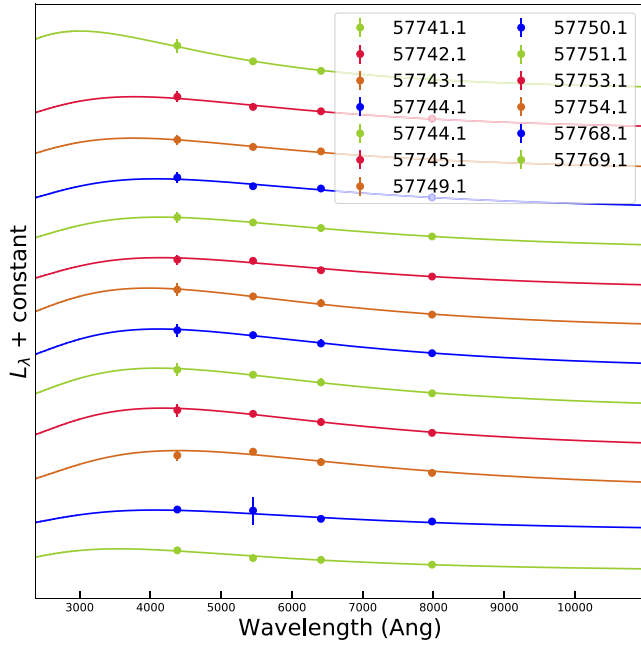


Figure A3. The black-body fits to the SED of SN 2016iyc to estimate the bolometric light curve generated from SUPERBOL.

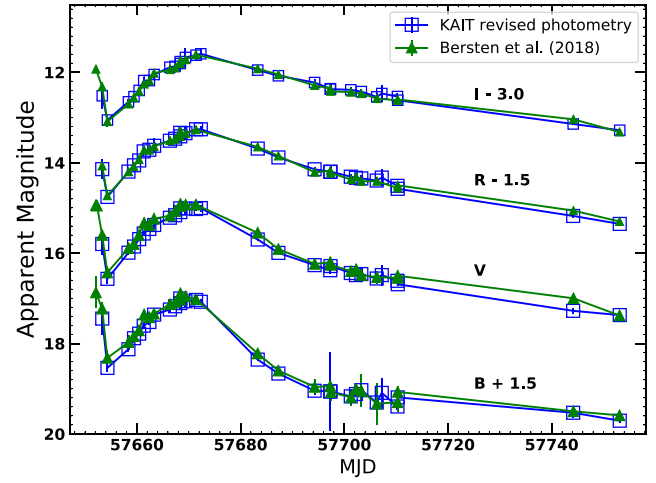


Figure A4. Comparison between the KAIT revised photometry and the KAIT data used by Bersten et al. (2018) for SN 2016gkg.

This paper has been typeset from a $\text{\TeX}/\text{\LaTeX}$ file prepared by the author.